

Copyright  
by  
Jinho Lee  
2002

The Dissertation Committee for Jinho Lee  
certifies that this is the approved version of the following dissertation:

**A UHV Variable Temperature STM and its Application  
to the Study of High- $T_C$  Superconductors  
and Carbon Nanotubes**

Committee:

---

Alex L. de Lozanne, Supervisor

---

John T. Markert

---

Chih-Kang Ken Shih

---

Qian Niu

---

John T. McDevitt

**A UHV Variable Temperature STM and its Application  
to the Study of High- $T_C$  Superconductors  
and Carbon Nanotubes**

by

**Jinho Lee, B.S., M.S.**

**DISSERTATION**

Presented to the Faculty of the Graduate School of  
The University of Texas at Austin  
in Partial Fulfillment  
of the Requirements  
for the Degree of

**DOCTOR OF PHILOSOPHY**

THE UNIVERSITY OF TEXAS AT AUSTIN

December 2002

To my parents, Sang Moo Lee and Seonja Kim,  
and to the late Y. Woo.

# Acknowledgments

Some researchers are fortunate to deal with nature's very basic elements - individual of them. I regard myself as one of those to have such chances by observing single electron transferred from the single atom through molecular structures.

First of all, I would like to thank professor Alex de Lozanne, my advisor, for this research opportunity, support, patience and insight. He always brings out new ideas and gives me guidance for transforming those abstractions to the implementations. I learned much from him not only physics itself but also importance of the interaction with other physicists. Through conversation with him, many problems I was struggling with for days presented itself as trivial. I also express gratitude to professor Ken Shih for allowing me to use his equipments, giving me many advice on STM, and professor John Markert for providing us of  $\text{YBa}_2\text{Ca}_3\text{O}_{6+x}$  single crystal samples and allowing me to use SQUID MPMS, furnaces etc. I also appreciate professor Zen Yao's guidance for the nano-scale physics, professor Michael P. Marder's superb condensed matter physics course and textbook, professor Qian Niu and professor John McDevitt for reviewing this dissertaion as my committee members. I also thank Zheong Gu Khim, my advisor for the M.S. degree, for allowing me to make a first step in the experimental condensed matter physics.

Our lab has a tradition. Whenever someone finishes his or her defense, Alex brings champagne and everyone cheers the graduation by drinking it together. The empty bottles are kept in the shelf on the corner of the lab. Now I count them eighteen. It's remarkable to think each bottle contains its own unique story and memory from outstanding minds who once lingered this lab. I feel myself lucky to meet many of such wonderfully talented people in this lab. All of them deserve the credit of not only my work, but also my joyful sojourn in this lab. Reflecting on them in chronological order- Dr. Minsun Yoo<sup>1</sup>, Dr. Scott Rubel<sup>2</sup>, Dr. Ulrich Purbach<sup>3</sup>, Dr. Chun-Che Chen<sup>4</sup>, Dr. David Derro<sup>5</sup>, Dr. Qingyu Lu<sup>6</sup>. I truly appreciate their help in every phase of my lab life, and wish them the best of luck.

I also feel lucky to have opportunity to meet many excellent visiting

---

<sup>1</sup>She was an amazing woman. I wondered where she gets all the energy to balance between roles as a housewife and a physicist. His husband, Minhoo Choi, gave me a ride when I came to Austin.

<sup>2</sup>I admire his intelligence and intuition. I remember he said "Don't expect your STM to run in one year after you start test." He was right. His joke was hilarious. Did I say he's intelligent?

<sup>3</sup>I miss his professionalism about the lab work. He was a very reliable, hard-working person, and one awesome Duke Nukem player. Also when I couldn't turn the frozen  $LN_2$  valve, he never failed me with his formidable grip.

<sup>4</sup>My smoke mate and starcraft mate. We talked a lot about everything. I respect his concentration and willingness to help other lab members. He gave me many crucial advices from his experience.

<sup>5</sup>He was my collaborator on this project. I wish him a good luck.

<sup>6</sup>He was a very energetic guy with an interesting background. I was always amazed by his confidence and readiness. He was the one who told me about the lab matters when I was a newbie. When I got stuck with some problem in experiment, he was also the one I always turned to first. I wish him a good health and a long life.

scholars and post doctorates. Dr. Xiang Dong Wang<sup>7</sup>, Dr. Tamotsu Koyano<sup>8</sup>, Dr. Yee-kin Tsui<sup>9</sup>. Of course the contemporaries deserve credit. Dr. Liuwen Zhang<sup>10</sup>, Dr. Ayan Guha<sup>11</sup>, Casey Israel<sup>12</sup>, Kevin Lee<sup>13</sup>, Jihoon Kim<sup>14</sup>, Tien-Ming Chuang, Junwei Huang, Sooeun Kim, Sung Soo Kim, Soo Hyun Phark.

There are also many people from the labs in RLM(The building we *live in*.) I would like to thank. Yunshik Lee, Dai Young Lim, Hoki Lyeo, Koki Mochizuki, Troy Messina, Casey Miller, Daejin Eom, Bonggu Shim, and Jonghyuk Kim, Yong Joong Lee. I'm also always amazed by the craftsmanship our machine shop crews possess. Alan Shroeder, and Jack Clifford & co. are truly walking encyclopedia of the machining. Whenever I got some machining project, they showed me the Tao of machining. I have many friends outside my direct academic field(whether they are in physics or not), but they have

---

<sup>7</sup>I bugged him asking bunch of questions about STM and he answered them with patience and mastery.

<sup>8</sup>I always feel I owe him a lot(and actually I do). Finally I can add the other pupil to the japanese wish doll "Daruma" he gave me. He also sent us  $\text{Bi}_2\text{Sr}_2\text{CaCu}_2\text{O}_{8+x}$  single crystal of the size of Texas.

<sup>9</sup>I learned a lot about cryogenics from him. I wish him to make his way to Hong Kong as he wishes. He also introduced me to  $\text{\LaTeX}$  I'm using.

<sup>10</sup>He is always sincere toward science, and showed me how to be a great coworker. I wish him a best of luck also in Tsinghua University. Believe it or not, his hobby was to read journals.

<sup>11</sup>I wish I had his knowledge of electronics and circuits. He conveys his ideas effectively and also clearly as do his caricatures.

<sup>12</sup>He was a very good listener and also showed creative ideas and ability to realize them. He and Dr. Zhang are a great duo.

<sup>13</sup>He kept growing his amazing carbon nanotube tips as an undergraduate, which became the main topic in my dissertation. Without him, this dissertation would have been of very different shape. He is now working in Dr. Yao's lab. pursuing Ph.D.

<sup>14</sup>Special thanks to him for the days and nights spent together during liquid  $^4\text{He}$  run trying to learn every aspects of the experiment. I wish him to have productive graduate career inheriting my STM.

been nonetheless influential. Suhan Lee, Sungyun Kim, Jung Hoon Lee, Unsuk Jung, Michael Ham, Yoon Suck Choi, and Seung Sang Oh, etc. I wish to thank all the people who helped me, but time would fail me to tell of . . .

My elder brother Jinseok Lee and my younger sister Yunsun Lee always gave me advice and moral, whenever I needed them, which I really appreciate. Finally, I would like to thank my parents, Sang-Moo Lee and Seonja Kim for their support and belief in me. They are wonderful parents.



# **A UHV Variable Temperature STM and its Application to the Study of High- $T_C$ Superconductors and Carbon Nanotubes**

Publication No. \_\_\_\_\_

Jinho Lee, Ph.D.

The University of Texas at Austin, 2002

Supervisor: Alex L. de Lozanne

The first part of this dissertation describes brief theoretical background for scanning tunneling microscopy (STM), single electron tunneling, and Coulomb blockade phenomena. The second part addresses issues on the design and construction of Ultra High Vacuum Low Temperature Scanning Tunneling Microscope (UHV LTSTM) and also its operation, the third part describes topographic, spectroscopic data obtained on high- $T_C$  superconductors and HOPG with carbon nanotube (CNT) tips with hitherto made UHV LTSTM system. The fourth part discusses on the possibility of new microscopy using CNT tip's remarkable  $I$ - $V$  characteristic.

Our UHV LTSTM can reach from room temperature down to  $\sim 8$  K. To control the STM head, we used W.A. Technology's TOPS<sup>®</sup> system and its software. STM experiments were carried out using double etched W wire

tips, and also carbon nanotubes grown on sharpened W wires. SEM images of these nanotube tips show bundles of SWNT or MWNT structures. Atomic-scale STM images on HOPG and 3 nm structural modulations on  $\text{Bi}_2\text{Sr}_2\text{CaCu}_2\text{O}_{8+x}$  crystals were observed with these nanotube tips. Rectifying  $I$ - $V$  characteristics with a threshold voltage of  $\sim 0.7$  V were observed with a nanotube tip and a  $\text{Bi}_2\text{Sr}_2\text{CaCu}_2\text{O}_{8+x}$  sample at 84K. This unexpected characteristics were explained in terms of double barrier tunneling. Quantized differential conductance peaks were also observed reproducibly with different carbon nanotube tips and different sample at different temperature from 13K to 84K, with peak to peak  $\Delta V$  as large as few 100 mV, which suggests coulomb blockade phenomena. Performing constant imaging tunneling spectroscopy(CITS) with these CNT tips with single electron box behavior, a new possibility of microscopy was discussed in virtue of Fourier transform.

# Table of Contents

<b>Acknowledgments</b>	<b>v</b>
<b>Abstract</b>	<b>ix</b>
<b>List of Tables</b>	<b>xiii</b>
<b>List of Figures</b>	<b>xiv</b>
<b>Chapter 1. Introduction</b>	<b>1</b>
1.1 Perturbation picture of STM . . . . .	2
1.2 Quantum point contact and Landauer formula . . . . .	4
1.3 Coulomb blockade . . . . .	8
<b>Chapter 2. Design and Construction of an UHV LTSTM</b>	<b>13</b>
2.1 Introduction . . . . .	13
2.2 System Design . . . . .	16
2.2.1 STM Head . . . . .	16
2.2.2 Radiation Shields and Shutters . . . . .	19
2.2.3 Versatile Manipulator and Tip-Sample Approach . . . . .	21
2.3 STM Construction . . . . .	24
2.3.1 Installing the STM Head in the Chamber . . . . .	24
2.3.2 Wire Connections . . . . .	25
2.4 Test and Operation . . . . .	27
2.4.1 Cooling Test . . . . .	27
2.4.2 Variable Temperature STM . . . . .	28
2.4.3 Test on HOPG . . . . .	30
2.4.4 Calibration of the Scanner . . . . .	33
2.4.5 Imaging of $\text{Bi}_2\text{Sr}_2\text{CaCu}_2\text{O}_{8+x}$ . . . . .	35

<b>Chapter 3. Carbon Nanotube as an STM Tip</b>	<b>38</b>
3.1 Introduction . . . . .	38
3.2 Growth of CNTs on a Tungsten STM Tip . . . . .	39
3.3 Tunneling with a CNT-STM Tip and a Double Junction Model	43
3.4 Coulomb Staircase . . . . .	48
<b>Bibliography</b>	<b>70</b>
<b>Vita</b>	<b>78</b>

## List of Tables

2.1	The result of the caibration for the piezo-tube scanner. . . . .	34
-----	--	----

## List of Figures

1.1	Narrow channel connecting two large electron gas reservoirs with chemical potential difference of $\delta\mu$ . . . . .	5
1.2	Equivalent circuit of single electron island coupled to a voltage source via two tunnel junctions where $n_1(n_2)$ is the number of electrons tunneling <i>into(out of)</i> the island via junction1(2). Each junction has capacitance and resistance. . . . .	8
1.3	The stability diagram of the single electron box in $V_a-Q_0$ plane. The central rhombuses correspond to the Coulomb blockade regions for different value of $n = n_1 - n_2$ . . . . .	11
2.1	STM head : (a) inner piezo tube, (b) outer piezo tube, (c) quartz tube, (d) sample stage, (e) sample clamp, (f) Si diode thermo-sensor, (g) heating resistor, (h) grounded plate, (i) sample and tip holders, (j) sample-tip manipulator, (k) top plate, (l) cold finger, (m) Cu wire for thermal bridging, (n) bottom plate, (o) pivot point, (p) approach screw, (q) ruby ball, (r) springs, (s) tip clamp, (t) spring inside of the glass fiber sleeve, (u) threaded rod, (v) Al lock . . . . .	17
2.2	Schematic diagram of liquid N <sub>2</sub> and liquid <sup>4</sup> He dewar. An indium pad was used to reduce thermal resistivity in the interface between copper shield parts and he stainless steel dewars. . . .	20
2.3	STM head and shield in operation. Rotating manipulator B, sample and tip can be replaced easily. By raising the rod connected to the shutter, both outer and inner shutter can be opened and closed. The manipulator A is a versatile tool. For further information, see fig. 2.4 and read § 2.2.3. . . . .	22
2.4	Illustrated manipulator movements. <i>Universal joint action</i> makes this manipulator carry out several operations: approach, sample cleave, and STM head lock. The smaller picture shows the movement of the mechanical feed-through according to the manipulator positions . . . . .	23
2.5	Left : Indium pads on 4K shield. The $\phi$ 1.5 inch macor <sup>®</sup> pad can be seen in the center. Right : macor <sup>®</sup> pad housing all the wiring and pins which are insulated from the chamber by epoxy of high thermal conductivity . . . . .	25

2.6	Temperature change upon liquid $^4\text{He}$ transfer. T1 is on the sample stage and T2 is on 4K shield. The liquid $^4\text{He}$ transfer started at time 0. Little difference between two graphs shows good thermal connection between cold finger and the STM head.	28
2.7	Temperature change vs voltage applied to the $2.0\text{ K}\Omega$ resistor on the sample stage. The test was performed when the STM head is locked(red) and unlocked(blue) when $\text{LN}_2$ was used for cooling. When the head was unlocked, the heating curve slope changed and the waiting time changed, suggesting it takes longer to reach the equilibrium temperature. Also shown is the heating curve when liquid $^4\text{He}$ was used (black, crossed circle). In this case, the STM head was unlocked. The temperature can be varied from 15K to 80K. . . . .	29
2.8	HOPG images at room temperature(300K). Images in the left column (A),(B),(C) are taken in the atmospheric environment. Images on the right column (D), (E), (F) are taken inside the UHV chamber. These images were used for calibration purposes. . . . .	31
2.9	$13\text{nm} \times 13\text{nm}$ and $256\text{ pixel} \times 256\text{ pixel}$ map of a HOPG surface. The temperature was 83K and a carbon nanotube tip(chapter 3) was used. In general, a large FOV is necessary for a 2D fourier transform analysis. . . . .	32
2.10	The calibration of the piezo tube scanner at room temperature(300K). (A) For the $x - y$ calibration, a 2-dimensional fourier transform was used. The bright spot inside of the circle corresponds to $2.13\text{\AA}$ . (B) A histogram method was used for the $z$ calibration. The two peaks correspond to different layers of the HOPG. . . . .	33
2.11	(A)(B)(C) STM images of $\text{Bi}_2\text{Sr}_2\text{CaCu}_2\text{O}_{8+x}$ at 35K. (D) Typical differential conductance showing superconducting gap structure. . . . .	36
2.12	(A) SQUID measurement of the $\text{Bi}_2\text{Sr}_2\text{CaCu}_2\text{O}_{8+x}$ sample used. $T^c \sim 85\text{K}$ . $T^{ir} \sim 75\text{K}$ . (B)(C)(D) STM images of $\text{Bi}_2\text{Sr}_2\text{CaCu}_2\text{O}_{8+x}$ at 35K. perpendicular stripe shapes are visible. $V_{bias} = 400\text{mV}$ and $I_t = 80\text{pA}$ . . . . .	37
3.1	SEM images of a pile of carbon nanotubes grown on W tip. . .	40
3.2	SEM images of carbon nanotubes usable as STM tips. The scale including the black bars is 100 nm. The exact nature of the interface between the CNT and the W tip is under study.	42

3.3	Demonstration of STM experiments using CNT-STM tips. (a) STM image of HOPG using a carbon nanotube tip at 84 K. (b) $\frac{dI}{dV}$ on a $\text{YBa}_2\text{Ca}_3\text{O}_{6+x}$ single crystal surface at 27K. A clear superconducting gap is visible. (c),(d) Bigger field of view images of $\text{Bi}_2\text{Sr}_2\text{CaCu}_2\text{O}_{8+x}$ single crystal at 83K. $30\text{\AA}$ modulations are visible. . . . .	44
3.4	B. Two different cases of rectifying $I - V$ characteristics (a) on $\text{Bi}_2\text{Sr}_2\text{CaCu}_2\text{O}_{8+x}$ at 84K and (b) on HOPG at 27K. In (a), the threshold voltage( $V - t$ ) doesn't change much even when the feedback bias voltage is changed to -900 mV, while $V_t$ varies greatly as the tunneling bias changes-tip sample distance changes in (b). . . . .	45
3.5	Schematic tunneling diagram for two different diodes. (a) Schottky diode. Rectification of current occurs due to Schottky barrier formed between metal and semiconductor.(b) Resonant assisted tunneling mechanism. Between two insulating junction barriers, a metallic island is formed. Tunneling from the smaller barrier to the larger barrier is suppressed because no energy level is available in the diode, so that the effective barrier thickness becomes twice the original tunneling barrier plus the width of the island. . . . .	47
3.6	Coulomb blockade specific staircase I-V characteristics were observed as high as 83K. These I-V characteristics were independent of position on sample surface and averaged over 32 I-V curves. While changing the setpoint tunneling current, the frequency of conductivity( $dI/dV$ ) peaks doubled. This results from the change of tip-sample distance, which, in turn, changes the capacitance of one of two junctions. . . . .	49
3.7	( <b>A</b> ) Fitting of Coulomb blockade I-V characteristic to the orthodox theory. Spectroscopy was done on a HOPG sample in UHV at 14 K. Simplified 2 junction model in D was used and fitting parameters are : $C_\Sigma = 5.5 \times 10^{-19}F$ , $R_1 = 5.0 \times 10^5\Omega$ , $R_2 = 8.5 \times 10^7\Omega$ , $Q_0 = -0.3e$ , $T = 14\text{ K}$ . $C_\Sigma = C_1 + C_2$ . ( <b>B</b> ) Another Coulomb staircase with the same CNT tip. $C_\Sigma = 3.7 \times 10^{-18}F$ , $R_1 = 5.0 \times 10^8\Omega$ , $R_2 = 8.5 \times 10^9\Omega$ , $Q_0 = 0$ , $T = 19\text{ K}$ . ( <b>C</b> ) Schematic diagram of experimental setup. The inset is $\frac{dI}{dV}$ plots on the $\text{YBa}_2\text{Ca}_3\text{O}_{6+x}$ surface at 15 K along the spatial distance of 100 nm. ( <b>D</b> ) Simplified 2 junction model. $Q_0$ is the background charge on the single electron island which explains the shift of the blockade region with respect to zero bias in A. Also shown an SEM picture of the carbon nanotube STM tip. Black bar is 100 nm. . . . .	53



- 3.8 Various I-V characteristics from the double-junctioned CNT STM tips. Simulation results(blue empty dots) from the orthodox theory are also shown for comparison. The fitting parameters are : **(A)**  $C_1 = 1.0 \times 10^{-19} F, C_2 = 0.5 \times 10^{-19} F, R_1 = 9.0 \times 10^4 \Omega, R_2 = 1.1 \times 10^7 \Omega, Q_0 = -0.1e, T = 14K$ . **(B)**  $C_1 = 3.0 \times 10^{-19} F, C_2 = 5.0 \times 10^{-19} F, R_1 = 8.0 \times 10^6 \Omega, R_2 = 3.0 \times 10^8 \Omega, Q_0 = -0.23e, T = 13K$ . **(C)**  $C_1 = 1.0 \times 10^{-22} F, C_2 = 8.0 \times 10^{-20} F, R_1 = 3.0 \times 10^4 \Omega, R_2 = 2.0 \times 10^5 \Omega, Q_0 = -0.5e, T = 14K$ . **(D)**  $C_1 = 1.5 \times 10^{-19} F, C_2 = 2.2 \times 10^{-19} F, R_1 = 1.0 \times 10^6 \Omega, R_2 = 1.4 \times 10^8 \Omega, Q_0 = -0.43e, T = 15K$ . . . . . 56
- 3.9 A. Three dimensional  $\frac{dI}{dV}$  plots as a function of the bias voltage and the position of the carbon nanotube tip on a  $YBa_2Ca_3O_{6+x}$  surface at 15 K . The conductivity peaks don't change as the tip moves. The superconducting energy gap( $\Delta_{SC}$ ) can be calculated from the difference between the central blockade region size and the other blockade region sizes. B. Similar plot for Pr-Ir tip- $Bi_2Sr_2CaCu_2O_{8+x}$  system at 36K without CB behavior. 58
- 3.10 **(A)** Topographic profile corresponding to the black line on the image of HOPG on the right. The atomic rows are 2.1 Å apart. Note that red circles in the topographic image are on the hills. Feedback bias voltage was 1.4 V which is far from the central blockade region, and the tunneling current was 70 pA. Temperature was 80 K. **(B)** Two dimensional plot of  $\frac{dI}{dV}$  of CNT nanotube STM tip - HOPG system as a function of position and bias voltage. The I-V curve was taken along the line in A and  $\frac{dI}{dV}$  was calculated from it. At the topographic dip (a), the blockade region gets narrow. On the right, a similar plot of the simulation result is shown. For the simulation parameters,  $C_\Sigma = 2.0 \times 10^{-19}, R_1 = R_2 = 1.0 \times 10^8, T = 80K$  were used.  $Q_0$  is set to oscillate between  $0e$  and  $0.35e$ . **(C)** Conductivity plot as a function of x and y at the bias voltage of 260 mV. This bias is where the discrete conductivity peak can be mapped. Individual filled states can be seen. Note that blue circles are on valleys even though their positions are identical to the red circles in A. **(D)** Crystal structure of graphite surface. Due to the strong site asymmetry, triangular sublattice is visible in STM topography (  $\alpha$  and  $\beta$  sites ). . . . . 60

- 3.11 **(A)** Two dimensional plot of  $\frac{dI}{dV}$  of CNT nanotube STM tip - HOPG system as a function of position and bias voltage. Also shown is the topographic profile corresponding to the same scan line. **(B)** 3D topographic image where positions a, b, c are indicated. The bias voltage for the feedback in constant current topography was -40 mV and temperature was 83 K. b is at the top of an atom, c is at the dip. **(C)** Simulation result showing  $\frac{dI}{dV}$  vs.  $Q_0$ . At a,  $Q_0$  changes two cycles of  $-0.4e \rightarrow 0.0e \rightarrow 0.4e \rightarrow 0.0e \rightarrow -0.4e$ . At b.,  $Q_0$  is set to rapidly change in one direction. Due to single electron tunneling, whenever  $Q_0$  change exceeds  $0.5e$ , single electron tunneling occurs and  $Q_0$  is set back to  $-0.5e$ . Parameters for the simulations are :  $C_\Sigma = 4.3 \times 10^{-18}$ ,  $R_1 = 5.0 \times 10^6$ ,  $R_2 = 8.5 \times 10^8$ ,  $T = 83K$ . Comparing the simulation results to the experimental results in A, it can be seen that  $Q_0$  change is related to the electronic structure of the HOPG surface. . . . . 63
- 3.12 Fourier analysis of the CITS data. **(A)** Topographic image during a CITS scan using a carbon nanotube STM tip. Each atom appears to be an ellipse due to the drift of the tip while performing CITS. Blue dots represent peak positions. The bias voltage is -40 mV and  $T = 83K$ . **(B)** The squared amplitude of the fourier-transformed differential conductance,  $\frac{dI}{dV}(f_v)$  along the black line  $x_1, x_2$  is plotted as a function of the  $f_v \propto \frac{1}{V}$  and the position. **(C)** The topographic profile along the line is also shown, and the color dots designate the asymmetric graphite atoms known as  $\alpha$  site atoms(red), and  $\beta$  site atoms(blue). **(D)** two dimensional plot of amplitude of each Fourier Transformed  $\frac{dI}{dV}$  curve of CITS as a function of x,y position at the specific frequency designated in B by white line at  $f_v = f_{vCB}$ . Red dots are the peak positions and can be identified as the  $\alpha$  atoms. Refer to the profile in C. **(E)** Aligned together, red dots and blue dots from A and D form the honeycomb lattice which is the actual order of the HOPG bulk. **(F)** The contour plot of the frequency  $f_v m(V^{-1})$  which gives the peak squared fourier amplitude  $|\frac{dI}{dV}(f_v)|^2$  the maximum value, as a function of x and y. This map represents the change of the capacitance  $C_2$  between the CNT tip and HOPG surface during scan. The dark areas surrounded by yellow contour lines are the minima which is located inside the honeycomb lattice designated by the white dots. Also notice that most of the maxima(brighter sites surrounded by green lines) corresponds to the  $\alpha$  atom sites. . . . 66

# Chapter 1

## Introduction

In 1981, a breakthrough in microscopy was made when the scanning tunneling microscopy (STM) was invented by G. Binnig and H. Rohrer [1] [2]. Since then, STM and its variations (dubbed scanning probe microscopy: SPM) have been applied to investigate myriads of surface phenomena not only in surface science, but also in various fields of science providing new *vision*. On the other hand, in 1978, a new field of condensed matter physics started when J. J. Thouless [3] pointed out that the size of a conductor, if made small enough, determines its electronic properties. Single electron tunneling ([4], [5] and references therein) was one of those discoveries resulting from the variety of theoretical and experimental research of mesoscopic phenomena. Yet another young field is blossoming from the discovery of carbon nanotubes (CNT) by S. Iijima *et al* [6], which followed the discovery of the Buckminsterfullerene ( $C_{60}$ ) [7] from the astrophysical study.

Our work benefits from these seemingly different, relatively new branches of physical sciences. Therefore, a brief description of some basic concepts will be presented before the main chapters.

## 1.1 Perturbation picture of STM

Since the scanning tunneling microscopy (STM) was invented [1], many theoretical schemes were developed and improved. Approaches using the Kubo-Greenwood formula [8], Lippmann's generalized Ehrenfest's theorem [9], Landauer-Büttiker formula [10] etc. are among those, and good review on them can be found in Reference [11]. The best known treatment is the perturbation method by J. Tersoff and D. R. Hamann [12] [13] using J. Bardeen's transfer Hamiltonian approach [14]. The tunneling current is given to first order in Bardeen's formalism by

$$I = \frac{2\pi e}{\hbar} = \sum_{\mu, \nu} f(E_\mu - E_F) [1 - f(E_\nu + eV - E_F)] |M_{\mu\nu}|^2 \delta(E_\mu - E_\nu), \quad (1.1)$$

where  $f(E - E_F) = (1 + e^{\frac{E - E_F}{kT}})^{-1}$  is the fermi function,  $V$  is the voltage applied to the sample,  $E_F$  is the fermi energy,  $M_{\mu\nu}$  is the tunneling matrix element between states  $\psi_\mu$  of the probe and  $\psi_\nu$  of the surface, and  $E_\mu$  is the energy of state  $\psi_\mu$  without tunneling. Bardeen made approximations: 1)  $\psi_\mu$  is real, 2)  $H\psi_\nu = E_\nu\psi_\nu$  within the surface and the barrier, 3)  $V_{tip}\psi_\nu \neq 0$  to show that

$$M_{\mu\nu} = \frac{\hbar^2}{2m} \int d\mathbf{S} \cdot (\psi_\mu^* \nabla \psi_\nu - \psi_\nu \nabla \psi_\mu^*), \quad (1.2)$$

where the integral is over any surface lying in the vacuum region. At small voltages and temperatures, 1.1 can be simplified,

$$I = \frac{2\pi}{\hbar} e^2 V \sum_{\mu, \nu} |M_{\mu\nu}|^2 \delta(E_\nu - E_F) \delta(E_\mu - E_F). \quad (1.3)$$

By approximating the tip as a point probe, the tip wave function is considered to be localized. In this case, the matrix element of 1.3 is simply proportional to the amplitude of the sample wave function  $\psi_\nu$  at the position  $\mathbf{r}_0$  of the tip, and the current reduces to

$$I \propto \sum_{\nu} |\psi_\nu(\mathbf{r}_0)|^2 \delta(E_\nu - E_F). \quad (1.4)$$

By noting the definition of the LDOS

$$\rho(\mathbf{r}_0, E) \equiv \sum_{\nu} |\psi_\nu(\mathbf{r}_0)|^2 \delta(E_\nu - E), \quad (1.5)$$

the right side of 1.4 is simply the surface local density of states (LDOS) at  $E_F$  or the charge density from states at  $E_F$ . This argument delineates the fact that the STM tunneling current is proportional to the sample surface LDOS at small bias voltage. In normal cases, it is fairly safe to consider the LDOS of the tip  $\rho_t$  and  $M_{\mu\nu}$  independent of the position relative to the sample. Therefore, using 1.5, we can rearrange the summation in 1.1 so that the current can be expressed in terms of the DOS's and single integral(or single summation),

$$I_{s \rightarrow t} = \frac{4\pi e}{\hbar} \int_{-\infty}^{\infty} \rho_s(\mathbf{r}_0, \varepsilon + eV) f(\varepsilon + eV - E_F) \rho_t(\varepsilon) [1 - f(\varepsilon - E_F)] |\mathbf{M}|^2 d\varepsilon, \quad (1.6)$$

where  $\rho_s, \rho_t$  are the LDOS of the sample and the tip respectively,  $\varepsilon = E - E_F$ , and  $\mathbf{M}$  is the tunneling matrix in 1.2. A factor of 2 is for the spin degeneracy and  $I_{s \rightarrow t}$  designates the current from the sample to the tip. Since there is also current in opposite direction, the tunneling current is given by,

$$I = I_{s \rightarrow t} - I_{t \rightarrow s} = \frac{4\pi e}{\hbar} \int_{-\infty}^{\infty} \rho_s(\mathbf{r}_0, \varepsilon + eV) \rho_t(\varepsilon) [f(\varepsilon + eV - E_F) - f(\varepsilon - E_F)] |\mathbf{M}|^2 d\varepsilon. \quad (1.7)$$

Substituting step functions for the fermi functions to simplify (i.e.  $T = 0$ ),

$$I = \frac{4\pi e}{\hbar} \int_0^{eV} \rho_s(\mathbf{r}_0, \varepsilon + eV) \rho_t(\varepsilon) |\mathbf{M}|^2 d\varepsilon, \quad (1.8)$$

To see the relation between the STM spectroscopy and 1.8, consider the case when the temperature is low and the tunneling matrix element is a constant. The tunneling current is proportional to the convolution of the tip and the sample's LDOS over an energy range  $eV$ .

$$I \propto \int_0^{eV} \rho_s(\mathbf{r}_0, \varepsilon + eV) \rho_t(\varepsilon) d\varepsilon. \quad (1.9)$$

Further assuming the tip DOS is a constant over the energy range of interest, the differential conductance is proportional to the LDOS of the sample [15].

$$\frac{dI}{dV} \propto \rho_s(E_F - eV + \varepsilon). \quad (1.10)$$

This simple case requires a special tip treatment to make a flat-DOS tip. On the other hand, a sample surface with known LDOS is easier to prepare than a reproducible tip. The tunneling spectra, therefore, can give information on the tip DOS. In this context, we studied our carbon nanotube STM tips's electrical properties by scanning comparatively well known surfaces in chapter ??.

## 1.2 Quantum point contact and Landauer formula

The quantum point contact is a static quantum mechanical potential, through which wave functions propagate or from which they reflect [16]. We

know that in any wire with resistivity larger than zero, energy dissipation occurs. On the other hand, wave propagation conserves energy. To resolve this controversy, Landauer [17] [18] pointed out that measuring conductivity of a system is to measure the voltage difference between two points in a circuit, that is, two reservoirs of electrons independently in thermal equilibrium but in different chemical potentials, which have been connected by the channel whose conductance is to be measured. Any electron transmitted through the channel has to give up energy once it arrives at the second reservoir, because the second reservoir is at a lower potential than the first. Dissipation occurs in the reservoirs. He also formulated the conduction in terms of transmission probabilities of propagating modes at the Fermi level. As shown in fig. 1.1, imagine two electron gas reservoirs having a slight difference  $\delta n$  in electron

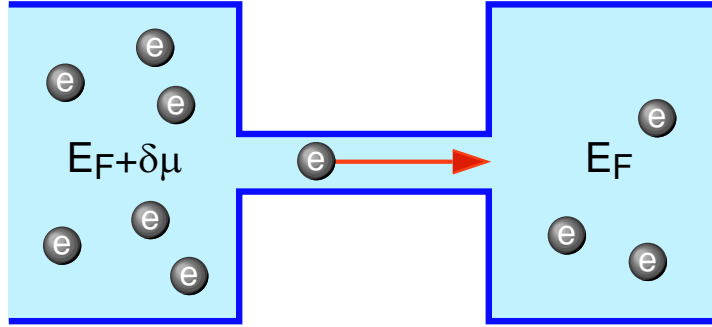


Figure 1.1: Narrow channel connecting two large electron gas reservoirs with chemical potential difference of  $\delta\mu$ .

density, which are connected via a narrow channel. A diffusion current  $J$  consisting of electrons with energies with energy  $E_F \leq E \leq E_F + \delta\mu$  will flow in the channel where  $\delta\mu = \frac{\delta n}{\rho(E_F)}$  is the Fermi energy difference,  $\rho(E_F)$  is the

DOS at  $E_F$  in the reservoir. The diffusion constant (or diffusance)  $\tilde{D}$  is defined by  $J = \tilde{D}\delta n$  and is related to the conductance  $G$  by

$$G = e^2 \rho(E_F) \tilde{D}. \quad (1.11)$$

1.11 generalizes the Einstein relation [19]. This diffusance is a function of  $E_F$  since the diffusion current is within a narrow range  $\delta\mu$  above  $E_F$ . One thing to note is that this current is caused by density differences, and not by electric field. With electric field, all electrons acquire a nonzero drift velocity regardless of their energy. Considering an ideal electron wave guide where the right moving electron states are occupied up to  $E_F + \delta\mu$ , while left moving electron states are occupied up to  $E_F$ . The diffusion current per energy interval carried by the right-moving states ( $k < 0$ ) in a mode  $n$  is the product of the density of states  $\rho_n^-$  and the group velocity  $v_n$ .

$$J_n = \int_{E_F}^{E_F + \delta\mu} dE g_s g_v (2\pi \frac{dE_n(k)}{dk})^{-1} \frac{dE_n(k)}{\hbar dk} = \frac{g_s g_v}{h} \delta\mu, \quad (1.12)$$

where  $g_s, g_v$  are for the spin degeneracy and valley degeneracy, respectively, and the DOS  $\rho^-(E)$  with  $k < 0$  per unit channel length in the  $n$ th 1D subband is given by [19],

$$\rho^-(E) = g_s g_v (2\pi \frac{dE_n(k)}{dk})^{-1}. \quad (1.13)$$

1.12 shows the amount of  $J_n$  is independent of mode index and Fermi energy. Namely, the current in the channel is shared equally among the  $N$  modes at the Fermi level since  $v_n$  and  $\rho^-(E)$  cancel each other [20]. This is the origin of the quantization of the conductance of a point contact. The linear response



conductance  $G$  of a mesoscopic structure is defined as

$$G \equiv \frac{I}{V}, \text{ in the limit } V \rightarrow 0. \quad (1.14)$$

Assuming  $g_s = 2, g_v = 1$ , and using 1.14, the conductance of this ideal wave guide is

$$G_{pc} = \frac{J_n}{\delta\mu} = 2\frac{e}{h}, \quad (1.15)$$

per channel, which is known as the conductance of a *quantum point contact*, where  $\frac{e}{h} = (25.8k\Omega)^{-1}$  is known as the *conductance quantum*( *resistance quantum* ).

If electrons are scattered within the channel, part of the injected electrons can be reflected back to the left reservoir. If a fraction  $T_n$  of  $J_n$  is transmitted to the reservoir at the right, then the total diffusion current in the channel becomes,

$$J = \frac{2\delta\mu}{h} \sum_{n=1}^N T_n, \quad (1.16)$$

where  $g_s = 2, g_v = 1$  are assumed. Using  $\delta\mu = \frac{\delta n}{\rho(E_F)}$ ,  $J = \tilde{D}\delta n$  in 1.11, we obtain the result

$$G = \frac{2e^2}{h} \sum_{n=1}^N T_n, \quad (1.17)$$

which can also be written as

$$G = \frac{2e^2}{h} \sum_{n,m=1}^N |t_{mn}|^2 \equiv \frac{2e^2}{h} Tr(\mathbf{t}\mathbf{t}^\dagger). \quad (1.18)$$

In the above relation,  $t_{mn}, \mathbf{t}$  are transmission probability amplitudes from mode  $n$  to  $m$ , and the corresponding matrix respectively. 1.18 is called as the *Lan-*

*dauer formula*. The identification of  $G$  as a *contact* conductance is due to Imry [21].

### 1.3 Coulomb blockade

Coulomb repulsion of the electron can become important as the size of electronic device becomes smaller. A measure of the importance of Coulomb repulsion is the charging energy  $\frac{e^2}{2C}$  of a single electron in the structure of the capacitance of  $C$ . This charging energy is not significant if the structure (*e.g.* quantum dot) is strongly coupled to the reservoirs, but it plays big role if the coupling is weak [22]. To describe this effect, consider a system consisting of a metal island connected to the voltage source via two junctions.

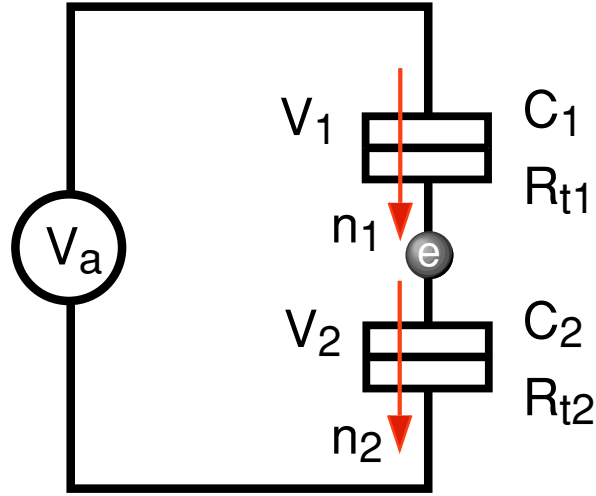


Figure 1.2: Equivalent circuit of single electron island coupled to a voltage source via two tunnel junctions where  $n_1(n_2)$  is the number of electrons tunneling *into(out of)* the island via junction1(2). Each junction has capacitance and resistance.

From fig. 1.2, each junction's charge( $Q_1, Q_2$ ) is related to the junction capacitance( $C_1, C_2$ ), and the total charge( $Q$ ) is the difference of these two charges:

$$\begin{aligned} Q_1 &= C_1 V_1, \\ Q_2 &= C_2 V_2, \\ Q &= Q_0 + Q_2 - Q_1 = Q_0 - ne, \\ n &= n_1 - n_2. \end{aligned} \tag{1.19}$$

where  $n$  is the net number of excess electrons on the island,  $n_1$  and  $n_2$  are shown in fig. 1.2, and  $Q_0$  is the residual charge present on the island [5]. We can write down  $V_1$  and  $V_2$  in terms of the applied voltage,  $V_a$  and the total capacitance of the island,  $C_\Sigma = C_1 + C_2$ .

$$\begin{aligned} V_1 &= \frac{V_a C_2 - Q}{C_\Sigma} = \frac{C_2 V_a + ne}{C_\Sigma}, \\ V_2 &= \frac{V_a C_1 - Q}{C_\Sigma} = \frac{C_1 V_a + ne}{C_\Sigma}. \end{aligned} \tag{1.20}$$

The electrostatic energy of the capacitors is

$$E_s = \frac{Q_1^2}{2C_1} + \frac{Q_2^2}{2C_2}. \tag{1.21}$$

Using 1.20, 1.21 becomes,

$$E_s = \frac{C_1 C_2 V_a^2 + Q^2}{2C_\Sigma}. \tag{1.22}$$

Also, work is done by the voltage source to transfer charge in and out of the island, which is  $W_s = \int dt V_a I(t) = V_a \Delta Q$ .  $\Delta Q$  is the total charge delivered by

the voltage source. When an electron tunnels through junction 2, the charge on the island becomes  $Q' = Q + e$  and  $n' = n - 1$ , and accordingly, 1.20, the voltage difference across junction 1 changes to  $V_1' = V_1 - \frac{e}{C_\Sigma}$ . From this we can notice the total displacement charge provided by the voltage source is  $\Delta Q = -\frac{eC_1}{C_\Sigma}$ . In similar way, we can derive  $\Delta Q$  when an electron tunnel through junction 1, and work done by voltage source when electron tunnel through junction 1 or 2 can be found as

$$\begin{aligned} W_s(n_2) &= -n_2 e V_a \frac{C_1}{C_\Sigma}, \\ W_s(n_1) &= -n_1 e V_a \frac{C_2}{C_\Sigma}. \end{aligned} \quad (1.23)$$

Now, we can express the total energy of the equivalent circuit in fig. 1.2 as a function of  $n_1, n_2$ .

$$E(n_1, n_2) = E_s - W_s = \frac{1}{2C_\Sigma}(C_1 C_2 V_a^2 + Q^2) + \frac{eV_a}{C_\Sigma}(C_1 n_2 + C_2 n_1). \quad (1.24)$$

From this, the condition for the Coulomb blockade can be found based on the change of  $E(n_1, n_2)$  as electrons tunnel through either junction [23]. At zero temperature (zero thermal fluctuation), system always changes toward the state with lower energy. When an electron tunnel through junction 1(2), the change in energy  $\Delta E_1$  ( $\Delta E_2$ ) of 1.24 is

$$\begin{aligned} \Delta E_1^\pm &= E(n_1, n_2) - E(n_1 \pm 1, n_2) = \frac{Q^2}{2C_\Sigma} - \frac{(Q \pm e)^2}{2C_\Sigma} \mp \frac{eV_a C_2}{C_\Sigma} \\ &= \frac{e}{C_\Sigma} \left[ -\frac{e}{2} \mp (ne - Q_0 - V_a C_2) \right], \\ \Delta E_2^\pm &= E(n_1, n_2) - E(n_1, n_2 \pm 1) = \frac{Q^2}{2C_\Sigma} - \frac{(Q \pm e)^2}{2C_\Sigma} \mp \frac{eV_a C_1}{C_\Sigma} \\ &= \frac{e}{C_\Sigma} \left[ -\frac{e}{2} \pm (ne - Q_0 - V_a C_1) \right]. \end{aligned} \quad (1.25)$$

Now, we may find conditions for blockade of tunneling putting the constraint that a transition occurs only if  $\Delta E_j^\pm > 0$ . From these four inequalities, we can draw a *stability plot* [24] in  $V_a, Q_0$  plane as shown in fig. 1.3 where the “Diamond shaped” blockade regions corresponding to each  $n$  is the region in which no tunneling current is allowed. This Coulomb blockade results from

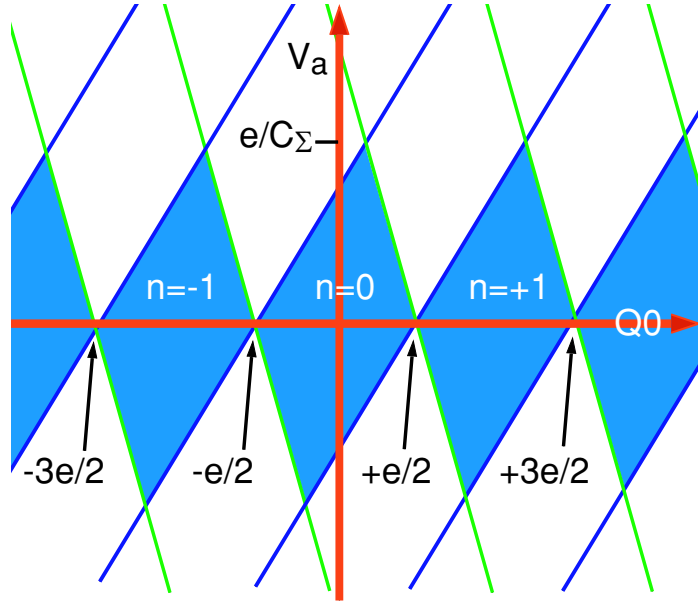


Figure 1.3: The stability diagram of the single electron box in  $V_a - Q_0$  plane. The central rhombuses correspond to the Coulomb blockade regions for different value of  $n = n_1 - n_2$ .

the Coulomb repulsion which appears as the additional Coulomb energy  $\frac{e^2}{2C_\Sigma}$  required in order to tunnel into the island.

There are two conditions to observe the well-defined Coulomb charging effect in the double-junctioned metal island [4] [25]. i) charging energy  $E_c = e^2/C_{island}$  should be greater than the thermal fluctuation, and ii) the quantum fluctuation of the particle number  $n$  is small so that the charge  $Q$  is well localized on the island. The second condition can be derived from the *uncertainty principle*  $\Delta E_c \Delta \tau_t > h$  where tunneling time constant can be roughly  $\Delta \tau_t \sim R_t C_\Sigma$ . In short, these conditions are:

$$\begin{aligned} E_c &\gg k_B T, \\ R_t &\gg \frac{h}{e^2} = 25.8 k\Omega. \end{aligned} \tag{1.26}$$

where  $\frac{h}{e^2}$  is already mentioned in § 1.2.

## Chapter 2

# Design and Construction of an UHV LTSTM

### 2.1 Introduction

Ultra high vacuum low temperature scanning tunneling microscopy (UHV LTSTM) has made a number of breakthroughs since its first appearance [26][27]. Low temperature STM study has several advantages. Contaminants are condensed and their chemical reactivity is reduced, which makes *in situ* cleaved sample surface cleaner and also makes the base pressure in the vacuum chamber lower (cryogenic pumping effect). Atomic processes are slowed down and we can minimize the phonon contribution to measured quantities as well as thermal noise. Furthermore, it is possible to study physical phenomena observable only at low temperatures, such as superconductivity, charge density waves (CDW), Friedel oscillation, and single electron tunneling (SET). Recent reports on high- $T_C$  [28] [29] [30] as well as vortices on NbSe<sub>2</sub> [31] proved LTSTM is truly a valuable tool to investigate surfaces of superconductors demonstrating its exceptional topographic and spectroscopic resolving power. On account of technological advances and new materials, nanosize structures can be fabricated and novel phenomena of such structures can be investigated. STM played a pioneering role in the study of such mesoscopic phenomena as a tool for the manipulation of individual atoms [32]. STM also made many dis-

coveries on nanostructures, as a probe especially in low temperature, examples of which are reports on  $C_{60}$  [33] and nanotubes [34] [35].

Thanks to those merits, even after about 20 years of history of STM, UHV LTSTM have been and will be built by quite a few groups. Recently, LTSTM systems using a cryostat [36], continuous flow cryostat [37], and  $^3\text{He}$  refrigerator [38] etc. have been constructed and successfully applied to various surface studies. These system showed mature state-of-the-art LTSTM designs.

Here we present a low cost UHV LTSTM system based on the cooling scheme described in reference [39] suitable for manipulating tips and samples from room temperature down to  $\sim 8\text{K}$ . Especially, temperature range of  $10\text{K} \sim 30\text{K}$  became of great interest in the study of  $\text{YBa}_2\text{Ca}_3\text{O}_{6+x}$  CuO chain structure since the cold cleaved ( $\leq 20\text{K}$ ) CuO-chain terminated surface of  $\text{YBa}_2\text{Ca}_3\text{O}_{6+x}$  single crystal loses the chain structures, if heated over 30-40 K range [40]. Our UHV chamber is equipped with a mechanical backing pump, a turbo-molecular pump, and ion ion/Ti-sublimation pump. The small STM head (  $\sim 5$  in. in diameter,  $\sim 1.7$  in. in height ) hangs from the bottom of the liquid  $^4\text{He}$  dewar, inside the two-fold radiation shields made of oxygen-free high-conductivity(OFHC) copper cylinders which connect to liquid  $\text{N}_2$  and liquid  $^4\text{He}$  dewars. For an easy replacement of tips and samples, and minimization of heat loss, an aluminum shutter was mounted on both shields. The inner shutter on the 4K shield (the OFHC copper shield connected to liquid  $^4\text{He}$  dewar) is carefully designed to accommodate superconducting magnetic solenoid in future. Locking the STM head to the 4K shield cools the head



down to  $\sim 8$  K. Manual approach was chosen for a fast approach, and for that purpose, double coaxial PZT-5H piezoelectric tubes were used for the scanners. This double piezo tube scheme also provides better matching of thermal expansion coefficient. Samples and tips can be easily changed by a specially designed manipulator hand with magnetic action load-lock rod. This LTSTM is relatively rigid, reliable, easy to operate and less costly. Details of the design and construction will be discussed and some test results will be presented in following sections.

## 2.2 System Design

The cryogenic nature of a LTSTM system makes its design demanding and its construction costly. Cu parts were used wherever high thermal conductivity is required. Easiness of changing samples and tips *in situ* is one of the key elements we considered in our STM design. For simplicity, we developed a two-stage manipulator capable of linear, rotational and swiveling motions by which multiple tasks - 1. Approach, 2. *In situ* cleaving of sample, 3. Locking STM head to the cold finger, 4. Moving tip position - are possible. To this purpose, parts of tiny, complex shapes and structures were designed and machined.

### 2.2.1 STM Head

High resonance frequency, in other words, *rigidity* is the first priority to consider in STM head design. It follows from the simple ideal case, that in STM with a perfect rigid body the only relative motion is the scanning of the tip on the sample. Making the STM head size small helps since  $\omega \propto \sqrt{\frac{m}{k}}$ , and usually the mass of the head  $\propto$  size of the head. Figure 2.1 shows schematics of our STM head design. To achieve large area scanning, 1.2 in. long quartered PZT-5H tube of outer diameter of 1/4 inch(fig. 2.1 a) was used for the scanner. To minimize thermal drift, another O.D. 3/8 inch PZT-5H tube with about the same length(b) was placed coaxially along the 1/4 inch PZT scanner. Both the PZT tubes have thickness of 20 mil. Since we approach tip to sample manually, clear view of tip and sample from the

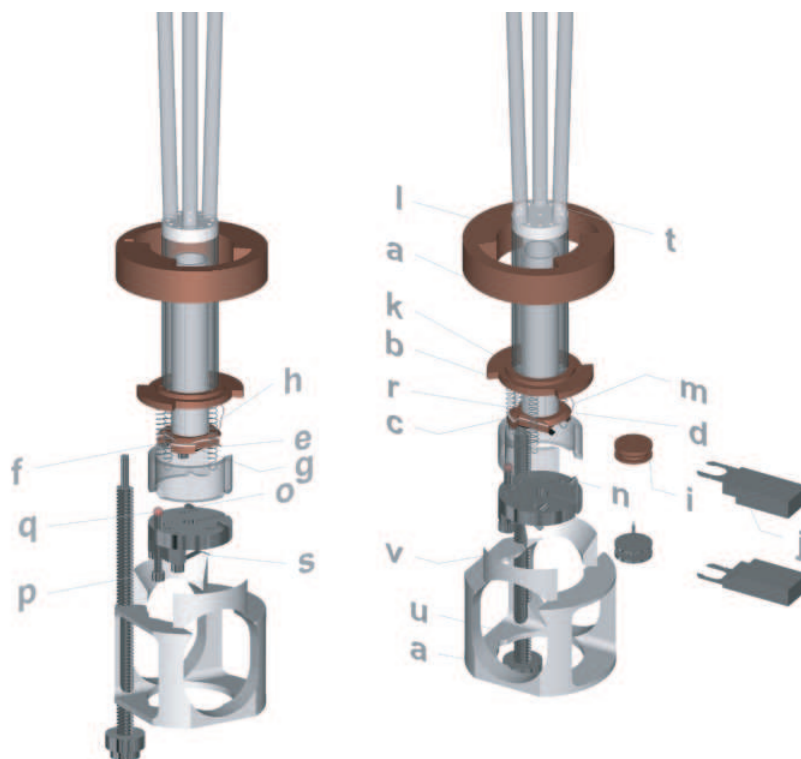


Figure 2.1: STM head : (a) inner piezo tube, (b) outer piezo tube, (c) quartz tube, (d) sample stage, (e) sample clamp, (f) Si diode thermo-sensor, (g) heating resistor, (h) grounded plate, (i) sample and tip holders, (j) sample-tip manipulator, (k) top plate, (l) cold finger, (m) Cu wire for thermal bridging, (n) bottom plate, (o) pivot point, (p) approach screw, (q) ruby ball, (r) springs, (s) tip clamp, (t) spring inside of the glass fiber sleeve, (u) threaded rod, (v) Al lock

outside of vacuum chamber is necessary. A quartz tube of 0.55 in. in O.D. and of a quarter in. in height(c) satisfied such demand providing excellent transparency and rigidity at the same time. Note also that quartz has about the same thermal conductivity( $\sim 10^3$  W/m K) [41] as sapphire( $\text{Al}_2\text{O}_3$ ) at 10K. The sample stage(d) in the STM head was miniaturized to be accommodated inside of the quartz tube. Figure 2.1-d is the sample stage made out of OFHC. Be-Cu alloy(Young's modulus  $Y \approx 1.3 \times 10^{11}$  Pa [41]) clamp(e) can hold the sample firmly and makes *in situ* sample change convenient. The bias voltage is applied via this clamp. A small carbon resistor of  $2\text{k}\Omega$  was attached to the side of sample stage by silver epoxy(Epotech<sup>®</sup> H21D) as a heater and OMEGA<sup>®</sup> CY-7 silicon diode thermometer was placed right next to the sample holder. Grounded plates were insulated from the high voltages of PZT tubes by Macor<sup>®</sup> or Torr-seal<sup>®</sup>. The sample holder and the tip holder(i) share virtually the same cylindrical geometry, and both of the holders can be mounted using simple manipulator hand(j). The top plate(k) has 2 fan shaped large areas which touch the cold finger(l) and act as a heat sink of whole STM head(fig. 2.3). A short wire of 10 mil in O.D.(m) is bridging between the top plate and the sample holder to provide direct heat flow from the sample to the cold finger compensating for the poor thermal conductivity of PZT tubes. This rather large diameter of the wire was selected within the calculated maximum Cu wire diameter which does not affect PZT-5H scanner movements. All Cu connections, all the way from the bottom of the dewar through OFHC pipe(fig. 2.2), and top plate, and finally to the sample are

achieved in this way. The bottom plate(n) can move up and down pivoting at (o) by turning down or up the 0-80 screw(p). At the end of the screw, a ruby ball(q) was attached to minimize friction between the screw and quartz tube. This lever reduction mechanism provides the main coarse approach in conjunction with applying voltage to the outer PZT tube to provide further vertical range of movement. To provide rigidity, 4 stainless steel springs(r) of O.D. of 60 mil(0.06 inch), fully extended within it's linear regime, connect the bottom plate to the top plate. Nonmagnetic stainless steel(SS 304) was used for the bottom plate to provide mechanical strength and durability. A Be-Cu alloy clamp(s) was bolted down on the bottom plate(n) to clip the tip holder easily. The head is hanging by 3 stainless steel springs for vibration and acoustic isolation, and each spring has a glass fiber sleeve(t) for mechanical damping and electrical insulation.

### 2.2.2 Radiation Shields and Shutters

Figure 2.2 shows the cooling system of our STM. The liquid  $^4\text{He}$  dewar is surrounded by a liquid  $\text{N}_2$  jacket from which it is separated by UHV. These shields are made of OFHC Cu pipes of thickness of 150 mil for the liquid  $\text{N}_2$  shield, and 65 mil(1/16 in.) for the liquid  $^4\text{He}$  shield. Silver soldering was used wherever necessary. On each shield, 2 windows were bored and filled with IR filtering Schott<sup>®</sup> glasses. The inner shield is also a cold finger in our design. Inside of this shield, we attached a contraption against which the head's Cu upper plate can be pushed(fig. 2.3. A cage-shaped Al lock(fig. 2.1) was made

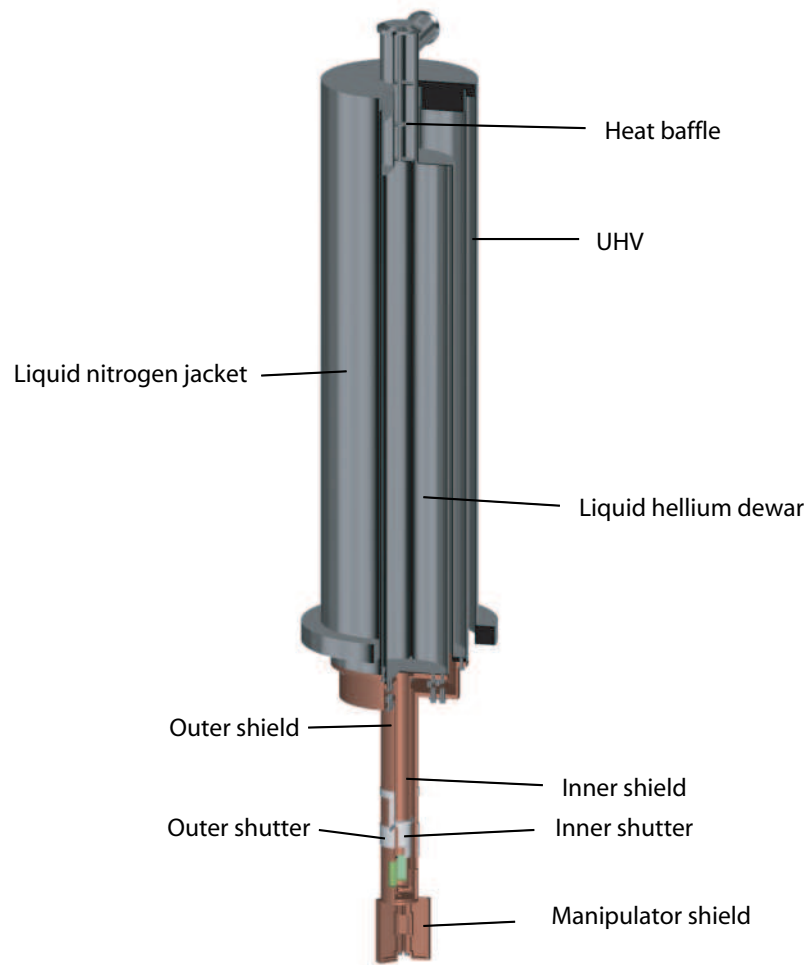


Figure 2.2: Schematic diagram of liquid  $N_2$  and liquid  $^4He$  dewar. An indium pad was used to reduce thermal resistivity in the interface between copper shield parts and the stainless steel dewars.

to engage/disengage the head to/from cold finger and also provide see-through so that manual approach is possible(see §2.2.3 for the actual operation of this lock). Locking the STM head to the cold finger accelerates cooling of the sample stage and enables sample and tip changes.

Another compact-like shield(fig. 2.3) was designed to shield the manipulator dangling below the 4K shield from the room temperature radiation. This shield consists of 2 parts, and can be opened and closed in butterfly-like way using the main manipulator. Bolting this to the liquid N<sub>2</sub> shield, all the parts connected to the liquid <sup>4</sup>He dewar are enclosed inside the 77K parts. Shutters were made of Al for both liquid N<sub>2</sub> and liquid <sup>4</sup>He shields. They can move vertically and be stopped at 3 positions by shutter rod and MDC<sup>®</sup> linear motion feed-through. During scan, both the shutters are placed at the lowest position and are disconnected from each other to thermally isolate the inner shield from the outer liquid N<sub>2</sub> shield.

### 2.2.3 Versatile Manipulator and Tip-Sample Approach

For reliable operation at low temperatures, we adopted a manual lever reduction mechanical approach. Fig. 2.4 shows two positions for the tip stage. By turning a fine 0-80 screw with a hex socket wrench, the tip can move a distance reduced by  $\sim \frac{1}{3}$ . Turning the screw by 5°, we can move tip up and down by  $\sim 1.5\mu\text{m}$ . Considering the combined total range of both PZT tubes( $\sim 1.6\mu\text{m}$  at 9K), approach can be done turning the 0-80 screw by 5° or less. To turn the 0-80 screw from the outside of the chamber, we adopted “*universal*

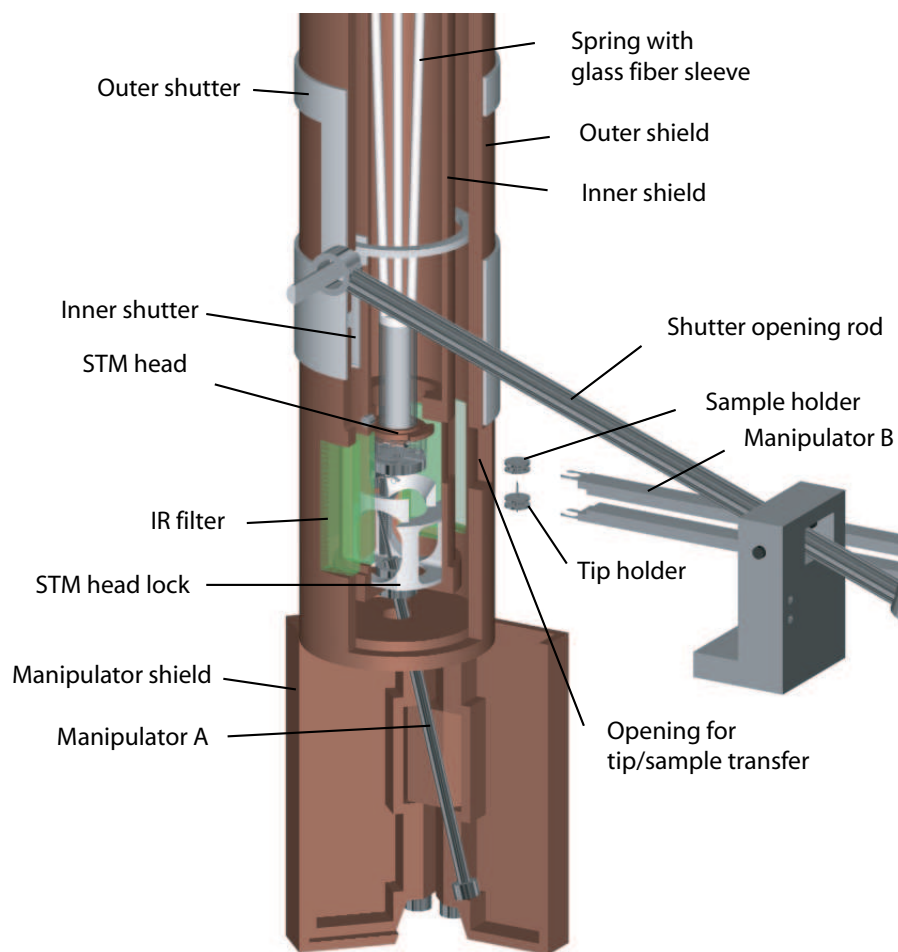


Figure 2.3: STM head and shield in operation. Rotating manipulator B, sample and tip can be replaced easily. By raising the rod connected to the shutter, both outer and inner shutter can be opened and closed. The manipulator A is a versatile tool. For further information, see fig. 2.4 and read § 2.2.3.



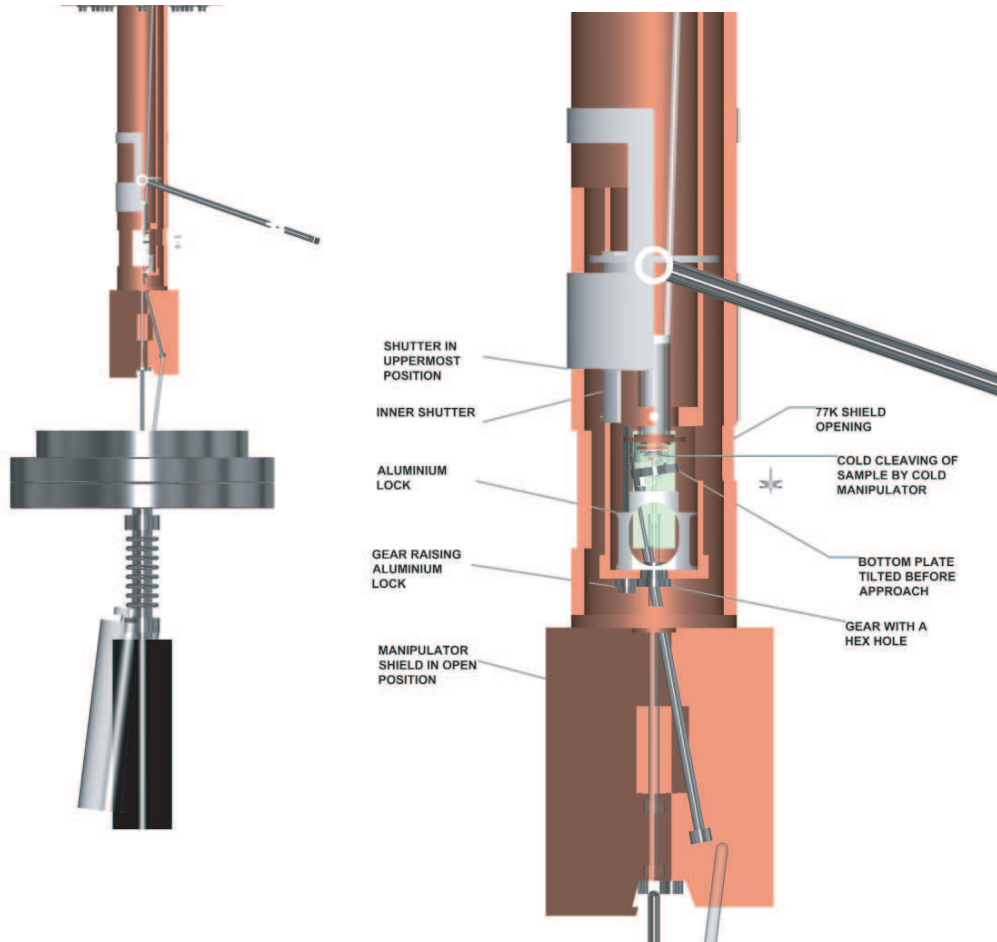


Figure 2.4: Illustrated manipulator movements. *Universal joint action* makes this manipulator carry out several operations: approach, sample cleave, and STM head lock. The smaller picture shows the movement of the mechanical feed-through according to the manipulator positions

*joint action*". A specially designed nonmagnetic stainless steel manipulator(50 mil manipulator) with a 50 mil allen key on the tip, as well as a  $\frac{1}{8}$ " hex key along its body, can move freely around a hole and is a truly versatile 2nd hand. Fig. 2.4 shows also this 50 mil manipulator's possible range of motion and position of MDC<sup>®</sup> feedthrough. This feed-through with a bellow is capable of linear, rotational, and angular motion. Engaging the small manipulator with this feed-through and moving it in a way a universal joint does, we can achieve multiple tasks by a single manipulator: 1. Approach, 2. *In situ* cleaving of sample[28][40], 3. Locking STM head to the cold finger, 4. Moving tip positions - are possible. Especially, since the 50 mil manipulator is contacting liquid <sup>4</sup>He shield and kept inside of the compact shield(fig. 2.4), cold cleaving of the sample is rather easy. To lock the head to the cold finger, one should fully withdraw the 50 mil manipulator which makes  $\frac{1}{8}$  hex key fit in a hex hole of a gear. In this position, rotation of the manipulator is delivered to the rotation of 4-40 thread rod(fig. 2.1) by gears, and as a result, the Al part(fig. 2.1-v) moves up and down.

## 2.3 STM Construction

### 2.3.1 Installing the STM Head in the Chamber

Two Cu radiation shields are bolted down to the bottom plates of the dewars using 8-32 bolts. Two helical spring washers were used in bolting of the liquid <sup>4</sup>He shield, to prevent possible loosening of bolts at low temperature. Indium pads (5 mils in thickness) were inserted between the shields and the

bottom plates of the dewars to provide a larger thermal contact area.

### 2.3.2 Wire Connections

At low temperature, heat loss through wires can be significant. For comparison, the heat leak of an object with an area of  $10\text{ cm}^2$  is about  $1.9 \times 10^{-3}$  Watts due to radiation from 77K to 4K, while heat leak due to conduction through 16 Cu wires of 3 mil in diameter is about  $7.8 \times 10^{-3}$  Watts assuming 10K difference of temperature. We designed a macor<sup>®</sup> plate for thermal anchoring of wires(fig. 2.5). All the wires from the head were lead through the space between two piezo tubes(fig. 2.1 a and b), through the insulating fiber glass sleeve, and soldered to the gold plated solder pads on top of the macor<sup>®</sup> plate. To electrically insulate the solder pads from the

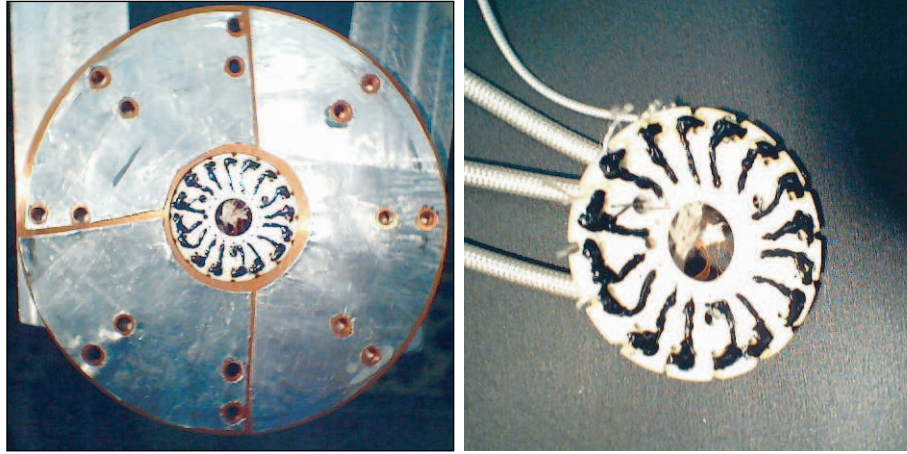


Figure 2.5: Left : Indium pads on 4K shield. The  $\phi$  1.5 inch macor<sup>®</sup> pad can be seen in the center. Right : macor<sup>®</sup> pad housing all the wiring and pins which are insulated from the chamber by epoxy of high thermal conductivity

dewar, Epotech<sup>®</sup> H77D (made of alumina powder, thermal conductivity of

$\sim 1 \text{ W/m}\cdot\text{K}$ ) was applied on top of the macor<sup>®</sup> plate. Again, Indium foil was applied between the epoxy and the dewar. For the wiring inside of the liquid  $^4\text{He}$  shield, Cu wires (thermal conductivity  $\sim 10^3 \text{ W/m}\cdot\text{K}$  around 13 K [41]) with 3 mil in diameter were used. The reason for using thin wires is to minimize vibrational coupling between the chamber and the STM head. Significant vibration can be coupled due to the boiling in the liquid  $\text{N}_2$  jacket. For the electrical connections between parts connected between the liquid  $^4\text{He}$  and the liquid  $\text{N}_2$  dewars, manganin (Cu-Mn-Fe alloy) wires were adopted because of its lower thermal conductivity ( $\sim 10^1 \text{ W/m}\cdot\text{K}$  at around 13K), 1/100 than that of Cu. In this way, Manganin wire reduces heat transfer from the liquid  $\text{N}_2$  shield and thermally anchored Cu wires inside of the liquid  $^4\text{He}$  shield contributes to cooling rather than heating of the STM head. The electrical wires from the liquid  $\text{N}_2$  shield to the electrical feed-through on the bottom flange are shielded with stainless steel braid except for a wire from the STM tip. Since the tunneling current signal (from pA to at nA) is prone to noise and cross talk with the high voltage wires, Microdot<sup>®</sup> connector (small coaxial cable compatible with high vacuum) was used for this STM tip wiring and connected to a separate feed-through right after which pre-amplification follows. To remove ground loops, all the grounding lines from the STM head were connected to the main chamber and then to the lab ground. Controlling electronics were grounded separately to the lab ground and not connected directly to the chamber. Also to reduce voltage drops between grounds, thick Cu or stainless steel braids were used, and chamber grounding was made close

to the feed-through for the tunneling current.

## 2.4 Test and Operation

### 2.4.1 Cooling Test

To keep the STM at low temperature, the liquid N<sub>2</sub> jacket of  $\sim 7$   $\ell$  in volume is filled once a day. The Liquid <sup>4</sup>He dewar of  $\sim 8$   $\ell$  in volume is filled with either liquid N<sub>2</sub> or liquid <sup>4</sup>He. If the liquid N<sub>2</sub> jacket is left unfilled for more than 28 hours, the temperature of the sample stage rises rapidly even though the inner dewar is filled with liquid N<sub>2</sub>. From this fact, we can clearly notice that radiation becomes a significant source of heat even at liquid nitrogen temperature. The following figure is a temperature vs. time graph after liquid <sup>4</sup>He transfer started. Within 1 hour, the sample temperature reaches around 10 K. A normal liquid <sup>4</sup>He transfer takes about 30 min or less. The red line is the actual temperature of the sample stage and the blue line in fig. 2.6 is readings by second thermo-sensor installed in the 4 K shield(fig. 2.3) for comparison. Around t=3.5 hours, the shutter was open halfway and the temperature went up by  $\sim 1^\circ$ . When the aluminum lock was released and the STM head was disengaged from the cold finger, the temperature stabilized around 13 K. Temperature of the inner 4K shield is stable at 8.5 K. For the liquid <sup>4</sup>He consumption, the first transfer required  $\sim 15$   $\ell$  and 7  $\ell$  afterwards if we refill the dewar every 24 hour. We found it takes about 36 hours to boil off dewar-full of liquid <sup>4</sup>He completely.

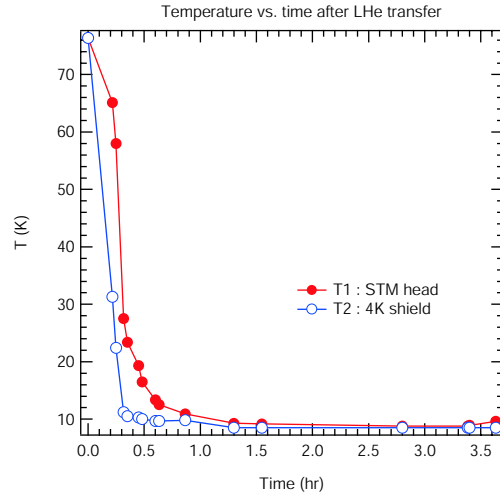


Figure 2.6: Temperature change upon liquid  $^4\text{He}$  transfer. T1 is on the sample stage and T2 is on 4K shield. The liquid  $^4\text{He}$  transfer started at time 0. Little difference between two graphs shows good thermal connection between cold finger and the STM head.

#### 2.4.2 Variable Temperature STM

Applying a DC voltage to the carbon resistor( $\sim 2k\Omega$ ) on the sample stage(fig. 2.7), we can vary temperature. The following graphs show the temperature vs voltage relations.

The graph shows roughly a  $V^2$  dependence. The red curves are when the STM head is locked to the cold finger and inner dewar(see fig. 2.2) is filled with liquid  $\text{N}_2$ . In this set up, change of heating time(5, 10, 15 minutes) didn't affect the curve due to the excellent thermal conduction. The blue curves are when the STM head is separated from the cold finger and liquid  $\text{N}_2$  was used. In this case, the slope of the heating curve changed noticeably at higher voltage applied to the heater, as heating time, namely applied amount

of heat, was varied from 10 to 15 minutes. This is an expected result since by disconnecting the STM head from the cold finger, the only thermal channels are through wires, springs, and radiation. Namely, the heat loss rate is less than the applied power. From this curve, we can roughly estimate the cooling rate when STM head is freely hanging. The two blue curves start to deviate around 3V which corresponds to a  $Power = \frac{V^2}{R} \approx 4.5mW$ . This value agrees with the thermal conduction rate through 16 wires in §2.3.2, considering a temperature difference of less than 10K. Since the STM head should be unlocked from the

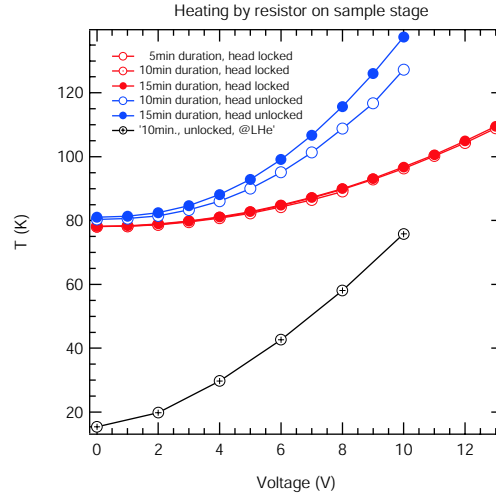


Figure 2.7: Temperature change vs voltage applied to the  $2.0\text{ K}\Omega$  resistor on the sample stage. The test was performed when the STM head is locked (red) and unlocked (blue) when  $\text{LN}_2$  was used for cooling. When the head was unlocked, the heating curve slope changed and the waiting time changed, suggesting it takes longer to reach the equilibrium temperature. Also shown is the heating curve when liquid  $^4\text{He}$  was used (black, crossed circle). In this case, the STM head was unlocked. The temperature can be varied from 15K to 80K.

cold finger and hanged freely when the STM is in scanning mode, the blue

curve simulates the more practical situation. This graph suggests that we have to wait longer to reach the stable temperature as we increase the heater voltage. The black curve with crossed circles is the heating curve of the STM head when liquid  $^4\text{He}$  was used. The measurement was performed with the head disconnected from the cold finger and the temperature became stable, simulating the actual liquid  $^4\text{He}$  run. In this case, the noise level increased noticeably as temperature increased probably due to the Seebeck potential resulting from the temperature difference on the wires, especially the wire from the tip.

### 2.4.3 Test on HOPG

Highly oriented pyrolytic graphite(HOPG) has many good properties for a STM test. It is easy to prepare since we can cleave HOPG in air and get an oxide-free surface. It is also known that STM images of HOPG show gigantic corrugations when small bias( $< 500mV$ ) is used [42], [43]. Our images of HOPG in Fig. 2.8 are taken at the room temperature(300K) for the purpose of the test and calibration. A larger field of view (FOV) scan is also shown in fig. 2.9. It is known that a large FOV map is advantageous for two dimensional fourier transform analysis [44].



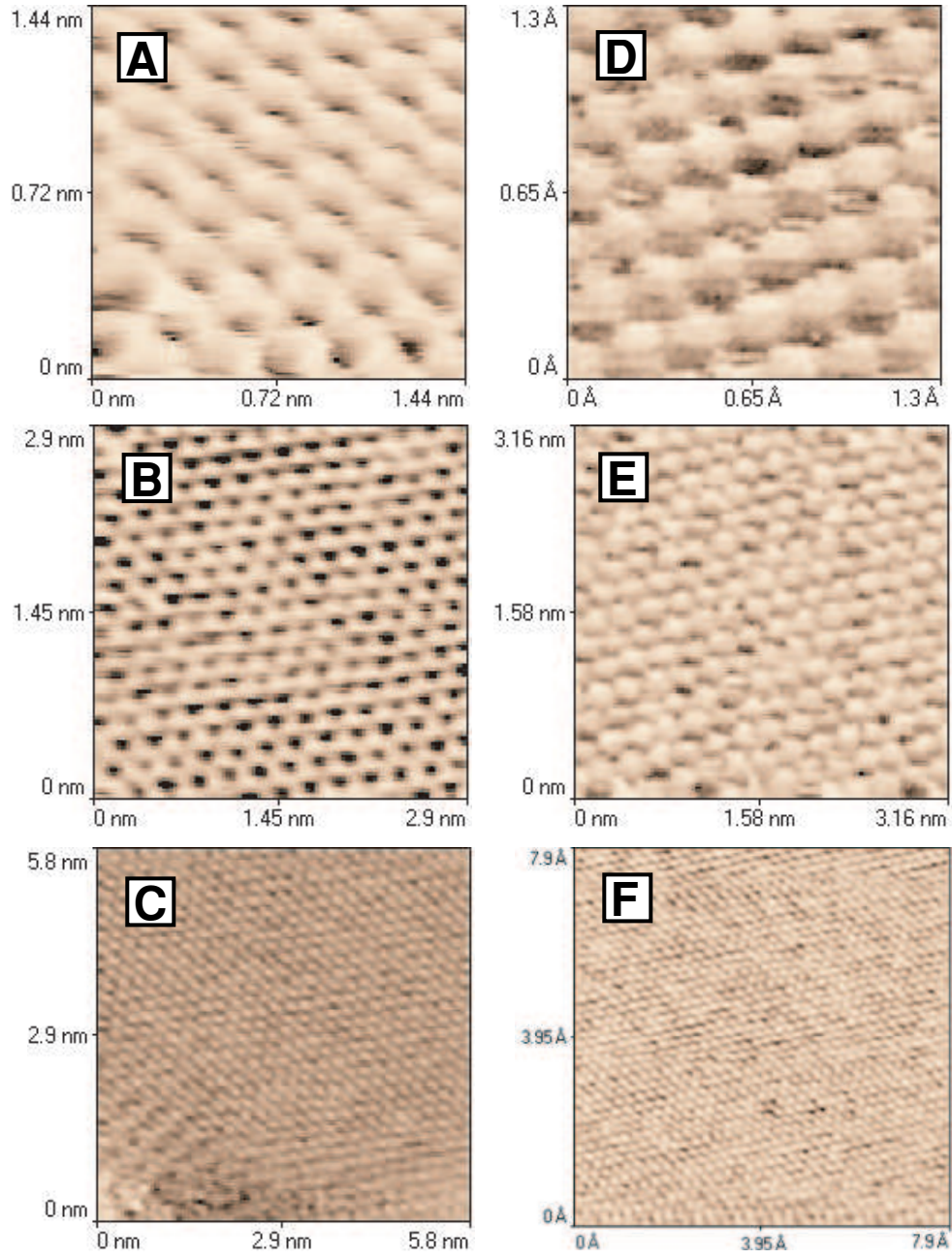


Figure 2.8: HOPG images at room temperature(300K). Images in the left column (A),(B),(C) are taken in the atmospheric environment. Images on the right column (D), (E), (F) are taken inside the UHV chamber. These images were used for calibration purposes.

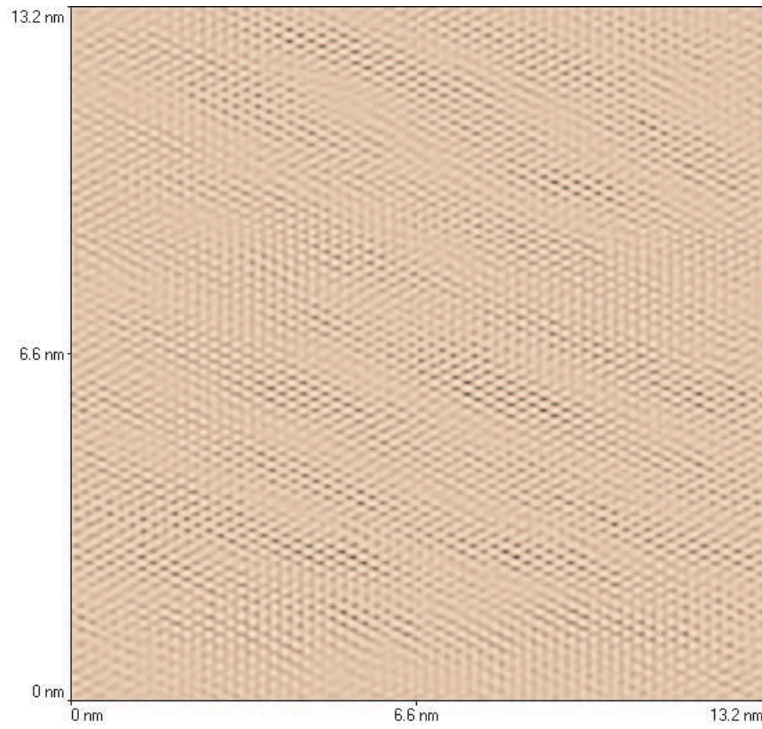


Figure 2.9:  $13nm \times 13nm$  and  $256 \text{ pixel} \times 256 \text{ pixel}$  map of a HOPG surface. The temperature was 83K and a carbon nanotube tip(chapter 3) was used. In general, a large FOV is necessary for a 2D fourier transform analysis.

#### 2.4.4 Calibration of the Scanner

The calibration of the piezo tube was done by scanning HOPG at room temperature(300K).

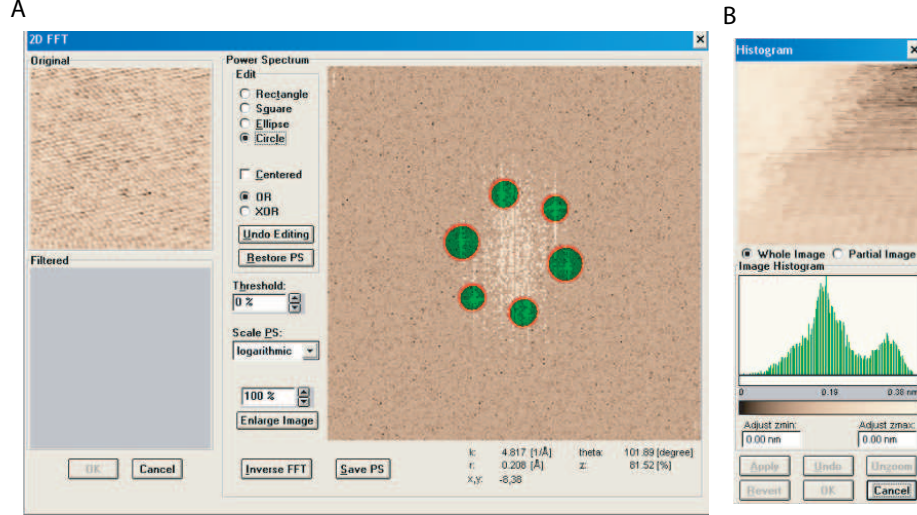


Figure 2.10: The calibration of the piezo tube scanner at room temperature(300K). (A) For the  $x - y$  calibration, a 2-dimensional fourier transform was used. The bright spot inside of the circle corresponds to  $2.13\text{\AA}$ . (B) A histogram method was used for the  $z$  calibration. The two peaks correspond to different layers of the HOPG.

For the  $x, y$  calibration, a two-dimensional fourier transform was performed to find the averaged lattice constant as shown in fig. 2.10(A). For the  $z$  calibration, we needed to find an area with a step edge, and then height distribution was surveyed to find averaged heights of different layers. Due to the large height difference of HOPG layers, clear imaging of each layers was difficult. From the fig. 2.10(B), two peaks correspond to  $1.9\text{\AA}$  and  $3.1\text{\AA}$  respectively, and from the difference of these two peaks, we extracted the nom-

inal height of one HOPG monolayer and compared it to the known value of  $3.35\text{\AA}$ . The value estimated by this method is consistent with the theoretical value given by 2.2. A similar method was adopted for the low temperature calibration and the result is summarized in table 2.1.

Table 2.1: The result of the caibration for the piezo-tube scanner.

	$K_x = \frac{\Delta x}{\Delta V} (\text{\AA}/V)$	$K_y = \frac{\Delta y}{\Delta V} (\text{\AA}/V)$	$K_z = \frac{\Delta z}{\Delta V} (\text{\AA}/V)$
300K	480	505	143
80 K	151	164	50

The sensitivity of the piezo tube can also be calculated from the *piezo-electric coefficient*  $d_{31}$  [15].  $d_{31}$  is defined as the ratio of the strain component over a component of the applied electrical field.

$$\begin{aligned} S_1 &\equiv \frac{\delta x}{x}, \\ d_{31} &\equiv \frac{S_1}{E_3}. \end{aligned} \quad (2.1)$$

We used a PZT-5H scanner from Staveley Sensors (EBL) which has  $d_{31}$  value of  $-2.74\text{\AA}/V$ . According to the reference [15], lateral and longitudinal piezo sensitivity is given by

$$\begin{aligned} K_x &= \frac{\Delta x}{\Delta V} = \frac{2\sqrt{2}d_{31}L^2}{\pi Dt}, \\ K_z &= \frac{\Delta z}{\Delta V} = \frac{d_{31}L}{t}. \end{aligned} \quad (2.2)$$

where  $L, D, t$  is the length, diameter, and thickness of the scanner, respectively. Using our scanner's specs ( $L = 1.2'', D = 0.25'', t = 0.020''$ ) in

2.2,  $K_{z,theory}$  is  $149\text{\AA}/V$  which matches our calibration result in table 2.1.  $K_{x,theory} = 305\text{\AA}/V$ , however, doesn't match well because of the large  $L$  of our tube-scanner which makes  $K_x$  deviate from the relation obtained from the linear approximation. The piezo sensitivity -  $\text{\AA}/V$  values were 3.1 and 3.6 times lower at 80K and 35K than that at room temperature, respectively. Again, we use a unipolar configuration by grounding two of the four quadrant electrodes of the scanner, which means we should divide  $K_x$  in ( 2.2) by 2 to make a correct comparison with our measured piezo sensitivity.

#### 2.4.5 Imaging of $\text{Bi}_2\text{Sr}_2\text{CaCu}_2\text{O}_{8+x}$

We also scanned  $\text{Bi}_2\text{Sr}_2\text{CaCu}_2\text{O}_{8+x}$  samples. Fig. 2.11 and fig. 2.12 show some of images of the surface of  $\text{Bi}_2\text{Sr}_2\text{CaCu}_2\text{O}_{8+x}$  taken at 35K. For the mounting and cleaving of the single crystal, we followed the same recipe for the  $\text{YBa}_2\text{Ca}_3\text{O}_{6+x}$  described in reference [40], and Pt-Ir or W tips were used. Typical values for the bias voltage and the tunneling current are  $\pm 100mV \sim \pm 400mV$  and  $50 \sim 100pA$ , but the positive bias is preferred in case of the W tip, because of the oxidization by oxygen removed from the  $\text{Bi}_2\text{Sr}_2\text{CaCu}_2\text{O}_{8+x}$  surface [45]. The  $30 \pm 5\text{\AA}$  modulation was observed.

Normally, a cleaved  $\text{Bi}_2\text{Sr}_2\text{CaCu}_2\text{O}_{8+x}$  single crystal surface terminates on an insulating BiO oxide layer [46] [47], but recently, there are reports on the observations of  $\text{CuO}_2$  terminated surfaces [45] [48]. Also there is a report on the observation of a four unit cell *checkerboard* pattern along the  $a$ - $b$  lattice inside the vortex [49].

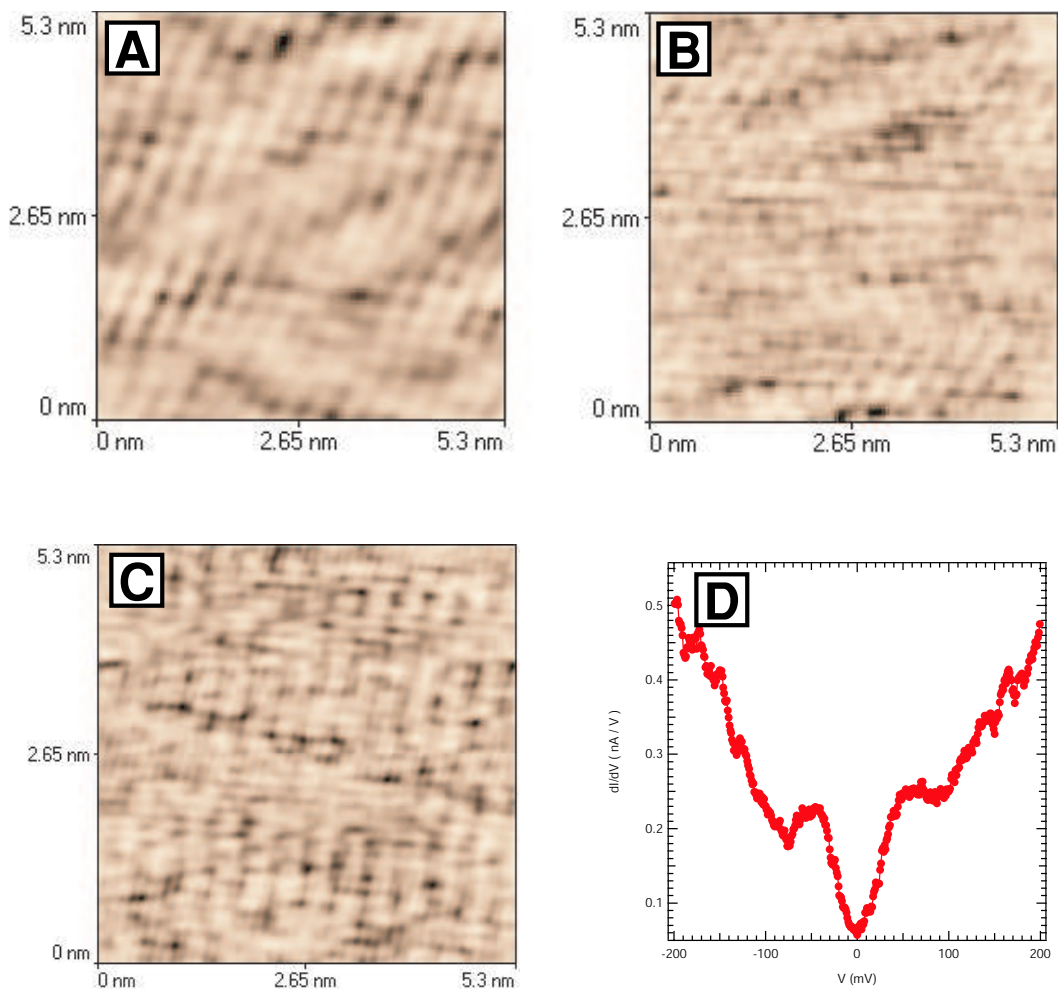


Figure 2.11: (A)(B)(C) STM images of  $\text{Bi}_2\text{Sr}_2\text{CaCu}_2\text{O}_{8+x}$  at 35K. (D) Typical differential conductance showing superconducting gap structure.



In our case, however, we observed a *checkerboard* pattern along the supermodulation directions. Fig. 2.12(B), (C), (D) show square modulation of charge density. This can be related to the aging of the sample( SQUID measurement in fig. 2.12(A) shows rather broad transition range of  $20K$ . ) and hence, deoxygenation of the  $\text{Bi}_2\text{Sr}_2\text{CaCu}_2\text{O}_{8+x}$  surface or change in surface structure, but the origin of these orthogonal modulations remains to be understood.

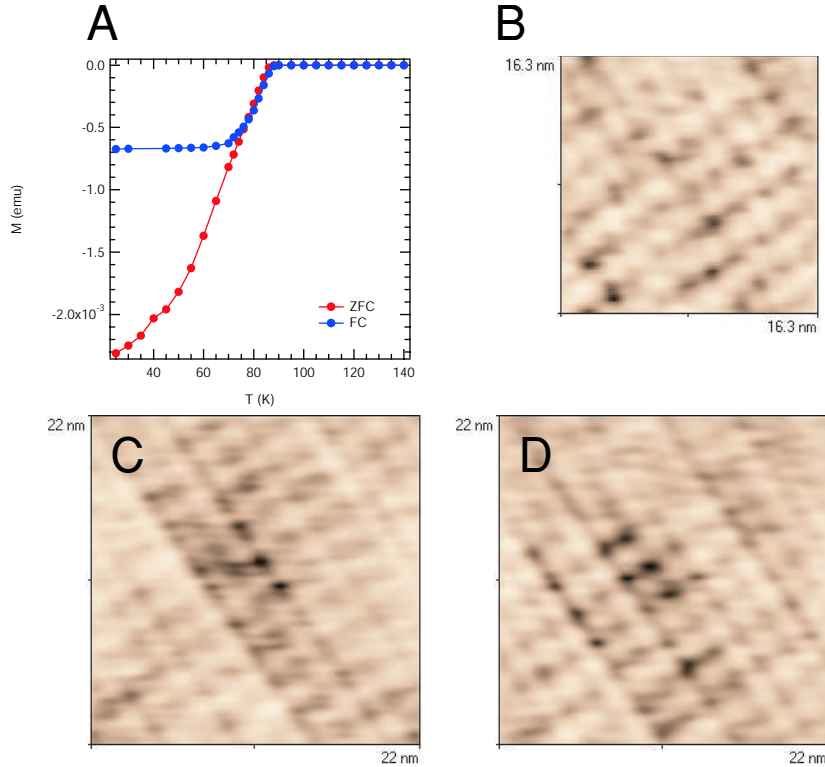


Figure 2.12: (A) SQUID measurement of the  $\text{Bi}_2\text{Sr}_2\text{CaCu}_2\text{O}_{8+x}$  sample used.  $T^c \sim 85K$ .  $T^{ir} \sim 75K$ . (B)(C)(D) STM images of  $\text{Bi}_2\text{Sr}_2\text{CaCu}_2\text{O}_{8+x}$  at  $35K$ . perpendicular stripe shapes are visible.  $V_{bias} = 400mV$  and  $I_t = 80pA$ .

## Chapter 3

### Carbon Nanotube as an STM Tip

#### 3.1 Introduction

When carbon nanotubes(CNT) were discovered, these sharp and strong, and at the same time resilient, conducting tips were more than welcomed by STM experimentalists as an alternative to the ductile conventional metal tips (W, Pt-Ir etc.). Some groups showed possibilities of using carbon nanotube tips as STM tips by picking up already made carbon nanotubes with a metal STM tip [50], but carbon nanotubes are used more frequently in scanning force microscopy [51] [52] than in STM nowadays due to such technical difficulties as vibration of the CNT, good ohmic contact between the CNT and metal tip, etc. Our first motivation of using a CNT as an STM tip came from the experience of the STM CVD technique. To write nano-wires using an STM tip, one needs a good field emitter with well defined sharpness. Carbon nanotubes seem very promising in this context. In this paper, we present a reproducible method for the synthesis of carbon nanotube STM tips and the STM experimental results using those tips.

Typical multi-wall nanotubes have a *diameter* of  $\sim 300$  Å [6], which can be compared to the practical limit of the *radius of curvature* of conventional



metal STM tips -  $\sim 500 \text{ \AA}$  [53]. From this fact, we can safely say all the carbon nanotubes are more than qualified for STM tip usage in terms of sharpness. The elastic modulus of a CNT is on the order of a Terra pascal [54], that is, CNT can withstand compression, buckling, tension and torsion without fracture [55] [56] which is a prerequisite for the tough STM operation, like in STM-CVD. The conductivity of a carbon nanotube is either metallic or semiconducting depending on its helicity (chirality) and diameter [34] [35]. In short, carbon nanotubes have every property required for the STM tip.

### 3.2 Growth of CNTs on a Tungsten STM Tip

We grew carbon nanotubes (CNT) on the end of the W tip by a catalytic CVD method [57]. Tungsten wires were etched in 12.5 M NaOH solution. For the best results, W tips must not be etched too sharp, as a sharp tip has little surface area, which reduces the chance of growing nanotubes. A radius of curvature of  $\sim 0.5 \mu\text{m}$  will do nicely. After etching, we clean the W tips in DI water using an ultrasonic cleaner. Next, to provide the catalyst, we electroplate these tips with Fe by dipping them into an iron nitrate solution for about a half second. A voltage of -2.030 V to -2.080 V gives the best results with a negative voltage applied to the tip and positive to the  $\text{Fe}(\text{NO}_3)_2$  solution.

Being ready to grow nanotubes, we put the etched and electroplated W tips in a tip holder which is connected to the positive electrode and insert the holder into a quartz tube furnace. The distance between the end of the

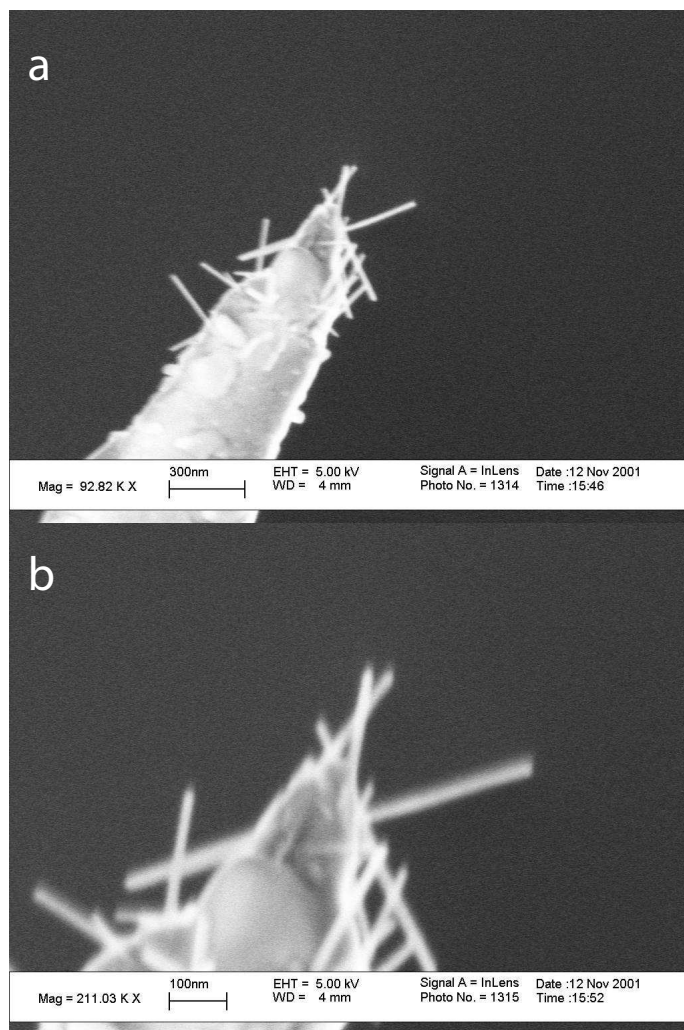


Figure 3.1: SEM images of a pile of carbon nanotubes grown on W tip.

tips and the negative electrode is crucial. Our optimized distance is  $\sim 4$  mm. About 295 V is applied by a DC power supply. Helium and  $H_2$  flow is opened before turning on the heater and when the gas flow becomes stable, the heater is started. It takes about 25 minutes to reach  $700^\circ\text{C}$ . After keeping the system at this temperature for at least 10 minutes, we turn on the  $C_2H_4$  gas and let it flow for about 20 min. The ratio of the flow rates of gases we used are  $\text{He:H}_2\text{:C}_2\text{H}_4 = 60:12:1$ . After stopping ethylene and hydrogen, turn off heater and allow it to cool to  $300^\circ\text{C} \sim 350^\circ\text{C}$  before opening the furnace door. The helium gas is stopped and the DC power is turned off after the quartz tube temperature reaches around  $150^\circ\text{C}$ . CNT's can be observed using SEM. Judging from the thickness of the CNTs, our CNT STM tips are either multi-walled or bundles of single-walled nanotubes.

To actually use these tips in STM experiments, we had to manipulate the tips very carefully since after high temperature treatment, the W tips become brittle due to the formation of tungsten carbide and W crystals. They can easily break. In our LT STM design, the tip wire should be slightly bent to provide friction between the tip and the stainless steel pipe(24 gauge) which is impossible with these CNT STM tips. Instead, we made a special tip holder which can hold the STM tips in a straight shape without bending them.

In fig. 3.2, some SEM images of such nanotube STM tips are shown. The most desirable CNT tip has a few short CNT's on the very summit of the tungsten tip. When CNT's were too long, due to vibration, it was not easy to get good resolution in the STM image. If the length of CNT was proper ( $\leq$

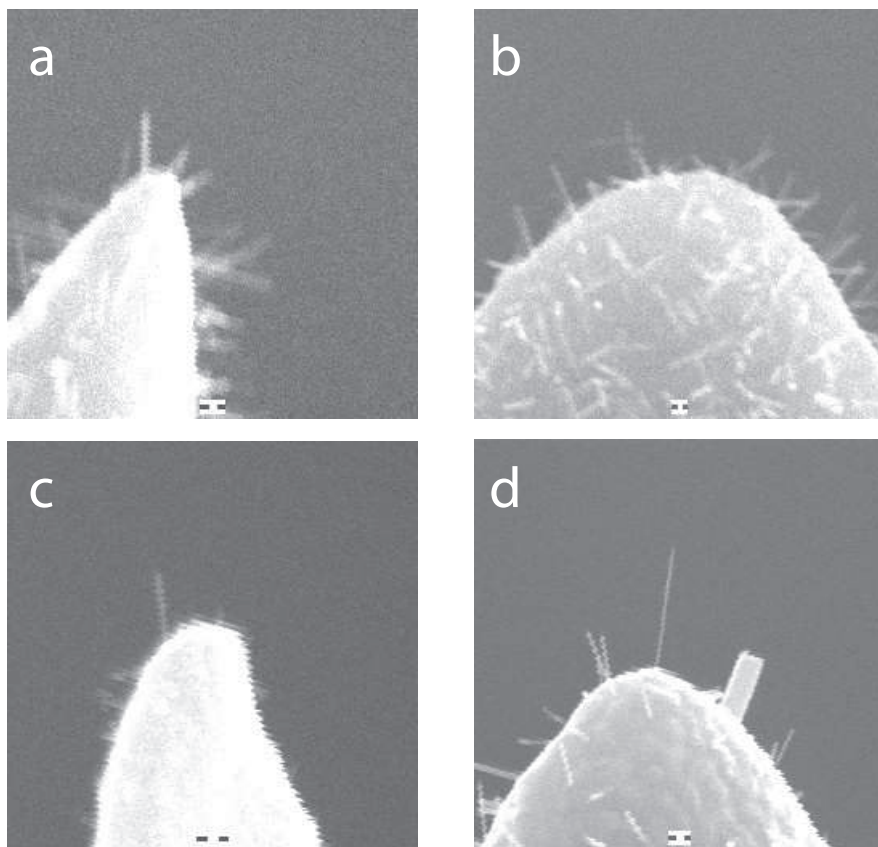


Figure 3.2: SEM images of carbon nanotubes usable as STM tips. The scale including the black bars is 100 nm. The exact nature of the interface between the CNT and the W tip is under study.

300 nm), even when the CNT tip interacted with the sample moderately, the approach distance did not increase as it does with a metal STM tips, showing exceptional elastic properties.

### 3.3 Tunneling with a CNT-STM Tip and a Double Junction Model

We have tested our CNT-STM tips successfully on various surfaces. Fig. 3.3(a) is an STM image taken on HOPG at 84K, (b) is differential conductance data showing gap structure of a  $\text{YBa}_2\text{Ca}_3\text{O}_{6+x}$  single crystal surface at 27K, and (c), (d) show images on vacuum cleaved  $\text{Bi}_2\text{Sr}_2\text{CaCu}_2\text{O}_{8+x}$  single crystal surface at 83K with CNT STM tips. All of these example demonstrate that we can use metallic CNT-STM tips for the usual STM operations. We found, however, in the CNT STM tip's case, tunneling signal noise was about 2 times bigger than noise in metal tip's case probably due to vibration. To minimize this noise, we had to increase the averaging of the tunneling signal per pixel to 32 (while it is usually averaged over 8 to 16 samplings).

Sometimes, we observed rectifying I-V curves as shown in fig. 3.4. It was intriguing at first, because when we used small negative tunneling bias, in certain cases, we lost the tunneling signal. We thought the CNT tip was broken at first, but withdrawing tip, changing bias to positive and re-approaching recovered the signal. Fig. 3.4 shows an example of such diode-like rectifying I-V characteristics. This rectifying behavior was independent of the position on sample and therefore, was due to the nature of the tip. There were 2 different

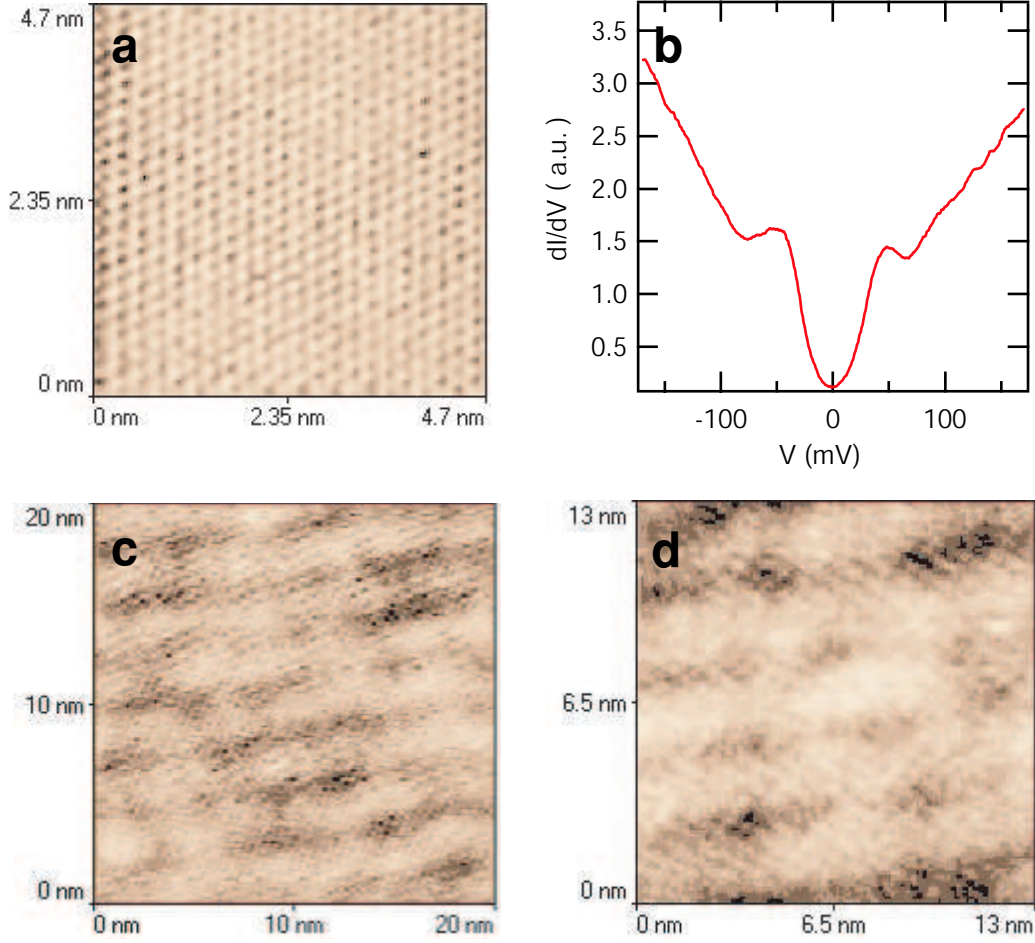


Figure 3.3: Demonstration of STM experiments using CNT-STM tips. (a) STM image of HOPG using a carbon nanotube tip at 84 K. (b)  $\frac{dI}{dV}$  on a  $\text{YBa}_2\text{Ca}_3\text{O}_{6+x}$  single crystal surface at 27K. A clear superconducting gap is visible. (c),(d) Bigger field of view images of  $\text{Bi}_2\text{Sr}_2\text{CaCu}_2\text{O}_{8+x}$  single crystal at 83K.  $30\text{\AA}$  modulations are visible.

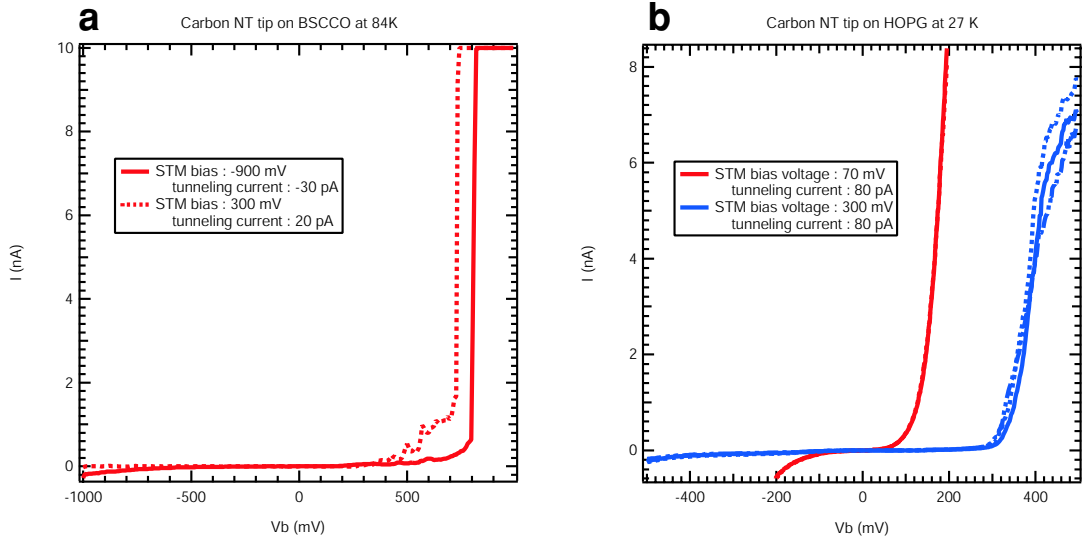


Figure 3.4: B. Two different cases of rectifying  $I - V$  characteristics (a) on  $\text{Bi}_2\text{Sr}_2\text{CaCu}_2\text{O}_{8+x}$  at 84K and (b) on HOPG at 27K. In (a), the threshold voltage ( $V - t$ ) doesn't change much even when the feedback bias voltage is changed to -900 mV, while  $V_t$  varies greatly as the tunneling bias changes-tip sample distance changes in (b).

types of rectifying I-V characteristics. The first case is shown in fig. 3.4 (a) where changing the bias voltage does not change the I-V significantly. Fig. 3.4 (b) shows, however, that the diode-like behavior changes greatly as the bias voltage varies and even loses rectifying characteristics to some extent. Currently, two possible mechanisms were suggested to explain diode-like behavior in carbon nanotubes and a metal interface. One of them is *Schottky Barrier mechanism* [58] where a semiconductor-metal interface is necessary. The other candidate mechanism is *Resonance-assisted tunneling* [59] [60] where a metallic island separated from two metallic electrodes by two junctions plays a role in the diode-like behavior.

Fig. 3.5 (a) depicts schematic tunneling diagrams for semiconductor-metal diodes. In such systems, changing the tunneling bias (changing the vacuum gap distance) does not change the threshold voltage of the diode which is the case in fig. 3.4(a). Applying this scenario to our case in fig. 3.4(a), a semiconducting CNT and metallic STM tip contact provides a Schottky barrier, and the tunneling vacuum gap between CNT and the sample provides single junction. Due to the large Schottky barrier, current through vacuum gap is blocked until it reaches threshold voltage. Namely, the  $I - V$  characteristic in fig. 3.4(a) is governed by the Schottky barrier on the CNT-STM tip. More interestingly, in fig. 3.5(b), a metallic island is formed between two barriers of different height and width for the general case. In case of a positive  $V_b$ , the threshold voltage is determined by the geometry, strength of the barriers and the level height inside of the island. Tunneling is resonantly enhanced when



the fermi level of left electrode coincides with that of the island. When  $V_b$  is negative, for tunneling to occur, carriers should tunnel through 2 barriers, and on top of that, there is no available energy level in the island for the tunneling, which suppresses tunneling further. In ref. [60], Chshiev et. al. used a Green function formalism to show that a strong asymmetric  $I - V$  similar to fig. 3.4(b) is possible by choosing appropriate parameters for the length of the middle island and the barrier heights in the M/O/M/O/M(M:metal, O:oxide) system.

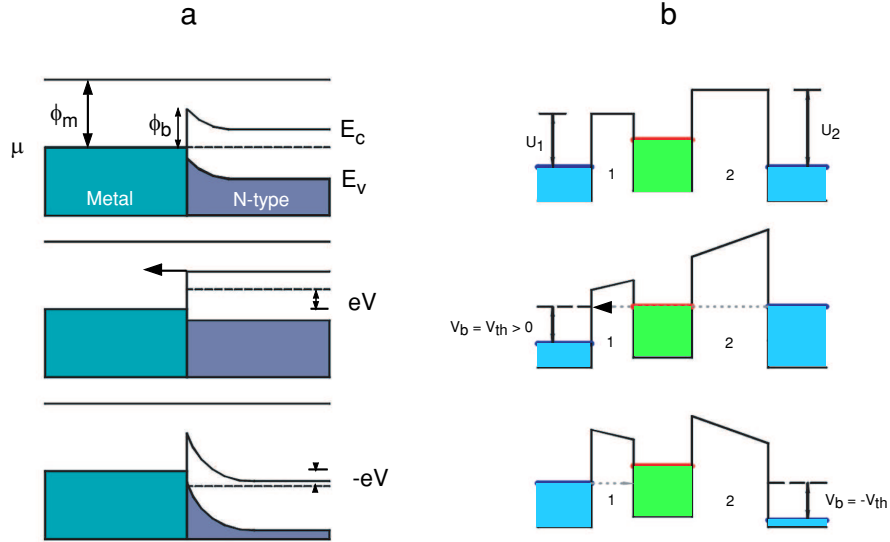


Figure 3.5: Schematic tunneling diagram for two different diodes. (a) Schottky diode. Rectification of current occurs due to Schottky barrier formed between metal and semiconductor.(b) Resonant assisted tunneling mechanism. Between two insulating junction barriers, a metallic island is formed. Tunneling from the smaller barrier to the larger barrier is suppressed because no energy level is available in the diode, so that the effective barrier thickness becomes twice the original tunneling barrier plus the width of the island.

### 3.4 Coulomb Staircase

More direct evidence of this latter mechanism came from other types of I-V characteristics. Fig. 3.6 shows step-like I-V characteristics showing coulomb blockade behavior [4] [5]. Coulomb blockade phenomena can be observed in systems similar to the model in fig. 3.4(b) where charges trapped in the island prevent tunneling by coulomb repulsion, even though the fermi level of one electrode is higher than that of island. Only when the energy difference is big enough to overcome the coulomb energy does tunneling occur. In many cases, we observed both rectifying I-V's and coulomb staircases from the same CNT tip by changing feedback bias and tip-sample distance, which implies that tunneling through two junctions is a good model.

There are two conditions for the coulomb blockade to be observed. [4] That is, the energy required to charge the island with a charge quantum should be larger than thermal fluctuation, and the junction resistance should be large enough to prevent tunneling without charging the island. The first condition,  $E_c > \frac{e^2}{k_B T}$  was checked using our experimental values. The temperature was 83K, which corresponds to about 10 aF. From other reports [61], typical capacitance of carbon nanotubes on a substrate is  $\sim 0.01$  aF/nm. If we adopt this value, we can observe coulomb blockade behavior on a CNT tip as long as  $1 \mu\text{m}$  at 83K. In fig. 3.6, the positions of the conductivity peaks can give us values for the characteristic capacitances:  $\sim 0.5$  aF and  $\sim 0.8$  aF for the solid line and the dotted line respectively. The second condition,  $R_t > \frac{h}{e^2} = 25.8k\Omega$  can be easily met in STM experiments because the usual junction resistance

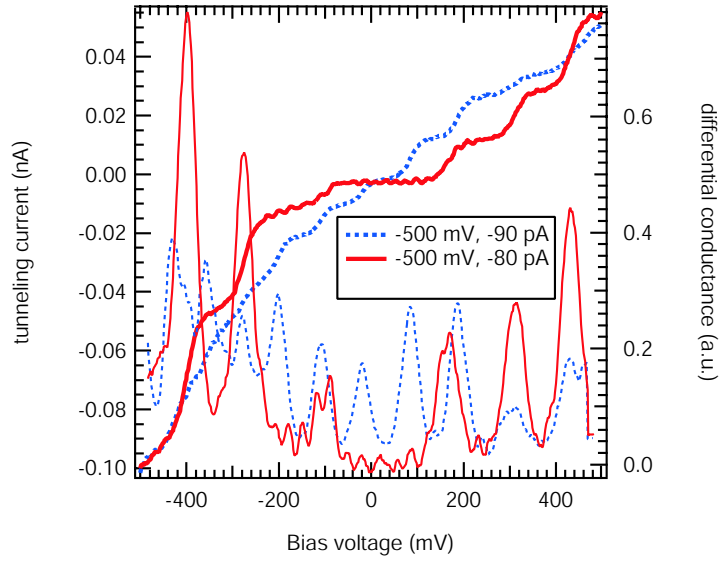


Figure 3.6: Coulomb blockade specific staircase I-V characteristics were observed as high as 83K. These I-V characteristics were independent of position on sample surface and averaged over 32 I-V curves. While changing the set-point tunneling current, the frequency of conductivity( $dI/dV$ ) peaks doubled. This results from the change of tip-sample distance, which, in turn, changes the capacitance of one of two junctions.

between a tip and a sample is of order of a giga ohm, provided the other junction of resistance greater than  $25.8\text{ k}\Omega$  is formed. Both graphs in fig. 3.6 are from the same cnt tip and the same sample, HOPG. Frequency doubling was observed as we changed tip-sample distance by adjusting tunneling current.

In summary, we successfully grew carbon nanotubes for use as STM tips, and demonstrated that these tips can be used as conventional STM tips in imaging and spectroscopy. Using CNT-STM tips, we also observed rectifying  $I - V$  characteristics of a different nature that are explained in terms of the schottky mechanism and a double barrier tunneling model, respectively. A strong Coulomb staircase  $I - V$  was also observed, which serves as direct evidence of double barrier formation in some of the CNT-STM tips. By engineering fine conditions of the CNT tip growth, we might be able to synthesize CNT-STM tips with desired  $I - V$  curves. We are currently working on CITS study of various surfaces using CNT-STM tips showing coulomb blockade behavior. Some of the early results will be presented elsewhere.

Coulomb blockade(CB) phenomena [4] have been investigated extensively using transport measurements [62] [63], STM [64] [65], and even adopted as a tool to survey charges and electric fields spatially with sub-micron resolution. The single-electron transistor scanning electrometer(SETSE) [66] [67] is one example of such devices which utilizes the well-known charge sensitivity(theoretically  $\sim 10^{-5} e$  [4], experimentally  $\sim 0.01 e$  [66] was reported.) of the single electron transistor device based on CB phenomena. Such SETSE has about 100 nm spatial resolution due to the size of the fabricated island at the end of the glass tip and topographic information cannot be obtained easily. On the other hand, after their discovery, carbon nanotubes(CNT) proved to be an ideal system to study CB [68] [69] as well as the physics of quantum wires or quantum dots. [70] In this context, the carbon nanotube is a promising candidate for the next generation of SETSE applications. CNTs have quite a few properties suitable for this purpose, such as being metallic(or semiconducting depending on the size and chirality), small radius of curvature, high Young's modulus, and junction formation by bending. [71] For the SETSE application of the CNT tip, however, there are some difficulties. Firstly, a CNT needs to be grown at the end of the conductive tip and be usable in scanning probe microscopy application. Another requirement is that at least one additional isolated electric lead needs to be connected to the CNT tip (in case of the AFM, 2 separate leads are required) to make a single electron transistor(SET) probe.

With the successfully grown CNT STM tips, we found another possi-

bility of microscopy by a different approach from that of SETSE. Here we present spectroscopic STM measurements as well as topographic measurements with atomic resolution using CNT tips with CB behavior, which suggest a novel type of scanning tunneling microscopy- Scanning Coulomb Blockade Microscopy(SCBM).

The variable temperature STM can be applied in the study of mesoscopic phenomena of not only samples but also of tips used for scanning. This is because the tunneling current is dependent on the convolution of the DOS of the sample and that of the tip. Since we succeeded in the growth of the CNT on the end of a W tip for STM use, a tunneling study of the nanotube vs various surfaces was possible. We tried HOPG,  $\text{Bi}_2\text{Sr}_2\text{CaCu}_2\text{O}_{8+x}$ , and  $\text{YBa}_2\text{Ca}_3\text{O}_{6+x}$  and observed coulomb staircase in all of those surfaces. For the growth of CNT on tungsten tip, we followed the catalytic CVD technique presented elsewhere and home-made variable temperature UHV STM system was used.

Fig. 3.7-A,B show fittings of I-V characteristics from the same CNT STM tip on the same cleaved HOPG surface, to the orthodox theory [5]. Current was measured directly since I-V is better for the CB fitting than dI-dV. Montecarlo method was used. For the fitting parameters, actual experimental conditions were used except for the island capacitances  $C_\Sigma = C_1 + C_2$ , and  $R_1$  which are unknowns to be determined from the fitting. Junction resistance  $R_2$  determines overall I-V slopes.  $C_\Sigma$  value of  $5.5 \times 10^{-19}F$  is rather small compared to the other STM measurements and transport measurements [61].

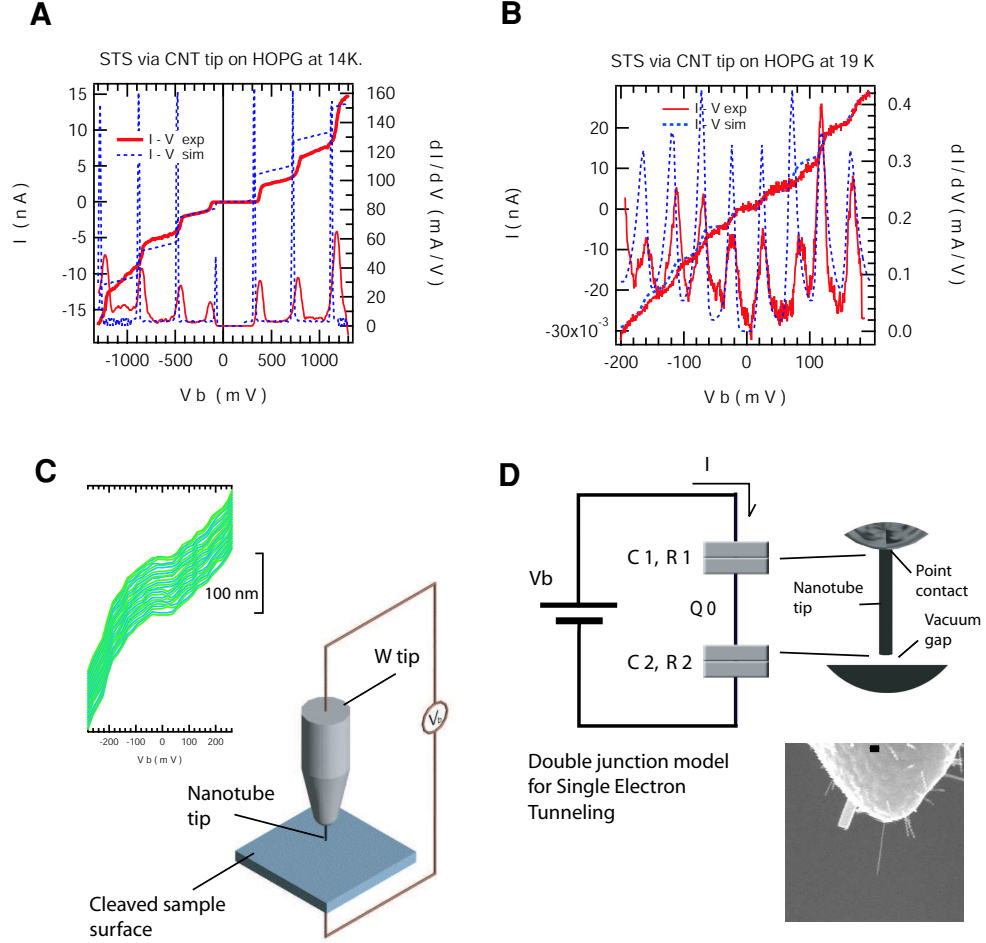


Figure 3.7: **(A)** Fitting of Coulomb blockade I-V characteristic to the orthodox theory. Spectroscopy was done on a HOPG sample in UHV at 14 K. Simplified 2 junction model in D was used and fitting parameters are :  $C_\Sigma = 5.5 \times 10^{-19} F$ ,  $R_1 = 5.0 \times 10^5 \Omega$ ,  $R_2 = 8.5 \times 10^7 \Omega$ ,  $Q_0 = -0.3e$ ,  $T = 14 K$ .  $C_\Sigma = C_1 + C_2$ . **(B)** Another Coulomb staircase with the same CNT tip.  $C_\Sigma = 3.7 \times 10^{-18} F$ ,  $R_1 = 5.0 \times 10^8 \Omega$ ,  $R_2 = 8.5 \times 10^9 \Omega$ ,  $Q_0 = 0$ ,  $T = 19 K$ . **(C)** Schematic diagram of experimental setup. The inset is  $\frac{dI}{dV}$  plots on the  $\text{YBa}_2\text{Ca}_3\text{O}_{6+x}$  surface at 15 K along the spatial distance of 100 nm. **(D)** Simplified 2 junction model.  $Q_0$  is the background charge on the single electron island which explains the shift of the blockade region with respect to zero bias in A. Also shown an SEM picture of the carbon nanotube STM tip. Black bar is 100 nm.

This can be understood in terms of simple electrostatic arguments. Overall step size  $\Delta V_{CB}$  is determined by  $C_\Sigma$  which is the capacitance of the island (fig. 3.7-D) [4]. In usual experiments, nanotubes are lying on a surface which makes capacitive area larger. In our case, a CNT tip grew at the end of the tungsten tip and capacitive area is about an order of magnitude smaller than when a nanotube is laid horizontally. Also in fig. 3.7-A, we found there were more than 2 orders of magnitude difference in two resistance values of  $R_1$  and  $R_2$  ( $\frac{R_1}{R_2} = 6 \times 10^{-3}$ ) which implies the fundamental difference between two junctions, which is natural since one junction is between nanotube and tungsten tip and the other junction is the vacuum gap. This strong asymmetry of the junction conductances makes only one oscillation period visible [5]. Since  $R_2$  is larger than  $R_1$  in our case,  $\Delta V \approx \frac{e}{C_2}$ . In short, we could observe the unusually sharp coulomb steps in fig. 3.7-A thanks to the two very different junctions formed in the nanotube STM tip tunneling setup, and the step size (oscillation period in conductivity) depends largely on the capacitance of the tunneling gap,  $C_2$ . The nature of the junction formed between the nanotube tip and the tungsten tip is not well known as of now but one possibility is a point contact between the carbon nanotube and the tungsten tip [19].

In fig. 3.7-B, the ratio  $\frac{R_1}{R_2}$  from the simulation fitting was about 0.06, the I-V curve was more rounded, and the oscillation period is about 7 times smaller than that of fig. 3.7-A. Since one nanotube tip can provide radically different coulomb blockade behavior even though vacuum gap is maintained, we can deduce that the characteristic of single electronic I-V curve largely depends on



the value of  $\frac{R_1}{R_2}$  and  $C_\Sigma$ . The cause of this radical change of  $\frac{R_1}{R_2}$  and  $C_\Sigma$  is not known well but we think mechanical change at the joint between nanotube and the tungsten tip, for example, by tip-sample interaction, can change these values significantly. Once the tip experienced a large change of this sort, it maintained about the same coulomb oscillation period, and a minute change of the CB step size was observed due to the small change in  $C_2$ . Over many Coulomb staircases, we observed the shift of the zero current blockade region around zero bias, which is the result of the background charge.  $Q_0$  [5] This effect will be discussed later in this report. Even though the island capacitance  $C_\Sigma$  is small, we did not observe tunneling spectra due to the energy levels of a quantum dot due to the length of the nanotube and rather high temperature.

It was only after this observation of the coulomb staircase in I-V, that we clearly understood the mechanism of myriads of different I-V curves carbon nanotube STM tips showed. Fig 3.8 shows some examples of fitting of very different I-V curves in context of the orthodox theory using the model system of an island with double junctions. It is remarkable that greatly different I-V's are possible as the double junction parameters on the CNT STM tips change. Rounding of the experimental curves results from the averaging over 32 I-V curves.

This coulomb blockade behavior was independent of the position, and especially strong CB was not beneficial resolution-wise. This is because the voltage range for the constant tunneling current gets too large due to the blockade region, and the CNT tip becomes less sensitive to the corrugations.

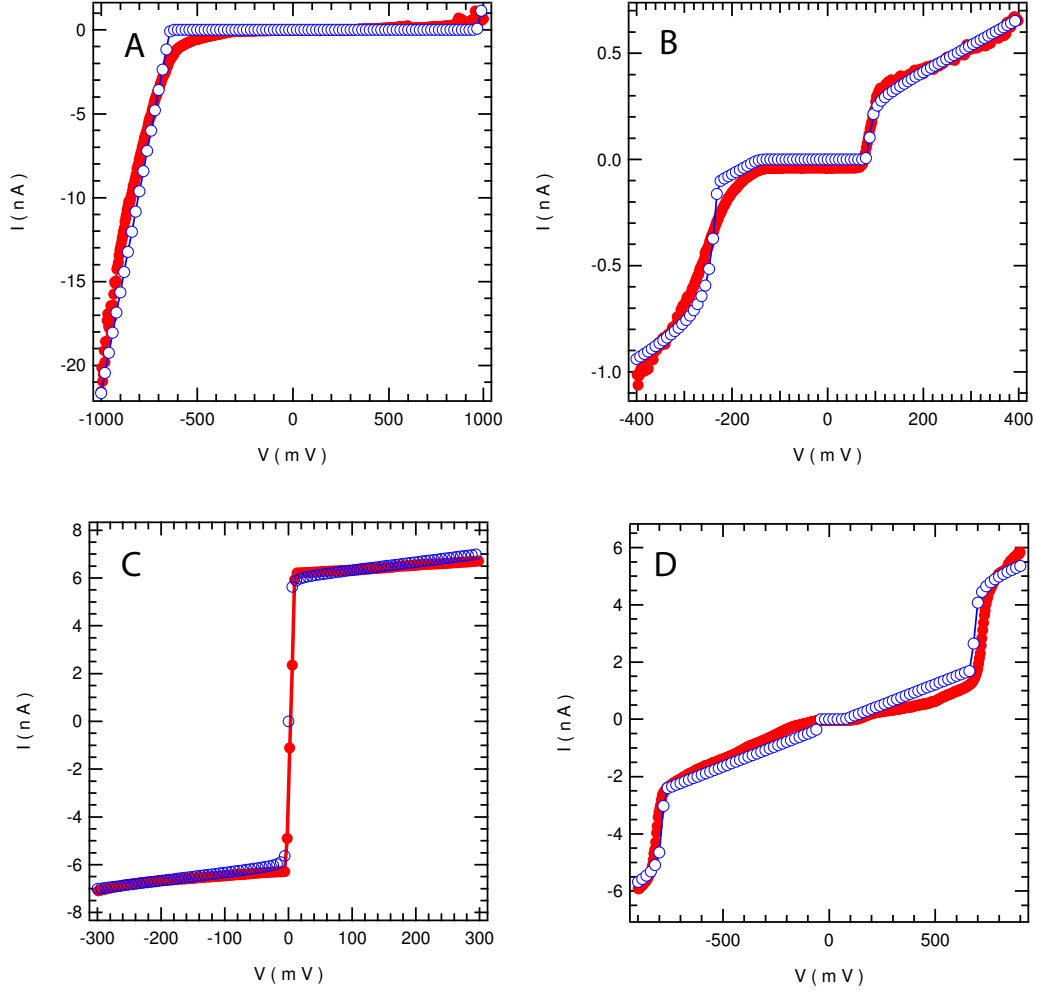


Figure 3.8: Various I-V characteristics from the double-junctioned CNT STM tips. Simulation results(blue empty dots) from the orthodox theory are also shown for comparison. The fitting parameters are : **(A)**  $C_1 = 1.0 \times 10^{-19}F$ ,  $C_2 = 0.5 \times 10^{-19}F$ ,  $R_1 = 9.0 \times 10^4\Omega$ ,  $R_2 = 1.1 \times 10^7\Omega$ ,  $Q_0 = -0.1e$ ,  $T = 14K$ . **(B)**  $C_1 = 3.0 \times 10^{-19}F$ ,  $C_2 = 5.0 \times 10^{-19}F$ ,  $R_1 = 8.0 \times 10^6\Omega$ ,  $R_2 = 3.0 \times 10^8\Omega$ ,  $Q_0 = -0.23e$ ,  $T = 13K$ . **(C)**  $C_1 = 1.0 \times 10^{-22}F$ ,  $C_2 = 8.0 \times 10^{-20}F$ ,  $R_1 = 3.0 \times 10^4\Omega$ ,  $R_2 = 2.0 \times 10^5\Omega$ ,  $Q_0 = -0.5e$ ,  $T = 14K$ . **(D)**  $C_1 = 1.5 \times 10^{-19}F$ ,  $C_2 = 2.2 \times 10^{-19}F$ ,  $R_1 = 1.0 \times 10^6\Omega$ ,  $R_2 = 1.4 \times 10^8\Omega$ ,  $Q_0 = -0.43e$ ,  $T = 15K$ .

If coulomb staircase steps are small, we could scan sample surface with almost as good resolution as normal STM tips. Another way is to choose bias voltage deliberately on the steep slope of the CB staircase, but in this case, tunneling current became highly sensitive to the noise, vibration of the tip etc. Fig. 3.9 shows three-dimensional plots of  $\frac{dI}{dV}$  as a function of bias voltage and position- A. is on  $\text{YBa}_2\text{Ca}_3\text{O}_{6+x}$  surface at 15 K whose surface was *insitu* cleaved in UHV where only periodic coulomb peaks independent of position due to the coulomb blockade are visible. Especially in this picture, the blockade region near zero bias is larger than other peak to peak step size which is the result of the superconducting gap of the  $\text{YBa}_2\text{Ca}_3\text{O}_{6+x}$  sample. Namely, for the quasi-particles to tunnel near zero bias, additional superconducting gap energy  $\Delta_{SC}$  is required on top of the single electron charging energy  $E_c = eV_{CB}$  of the CNT tip. Therefore, by subtracting the dominant step voltage  $V_{CB}(\sim 120 \text{ mV})$  from this central blockade region size ( $\sim 200 \text{ mV}$ ), we can obtain the magnitude of the  $\text{YBa}_2\text{Ca}_3\text{O}_{6+x}$ 's superconducting energy gap ( $2\Delta_{SC} \sim 80 \text{ mV}$ ) which yields  $\frac{2\Delta_{SC}}{kT_c} \sim 10$ . This result is consistent with other reports [72] considering our  $\Delta_{SC}$  is the peak to peak value in  $\frac{dI}{dV}$ . A similar plot on Pt-Ir STM tip-  $\text{Bi}_2\text{Sr}_2\text{CaCu}_2\text{O}_{8+x}$  system is presented for the comparison in fig. 3.9-B, where more detailed structures could be seen.

Since HOPG has a well known structure, stable surface, and easiness to obtain topographic image, it was our choice to test our CNT STM tip with double junctions.

To investigate the correlations of this I-V shape and the topographic

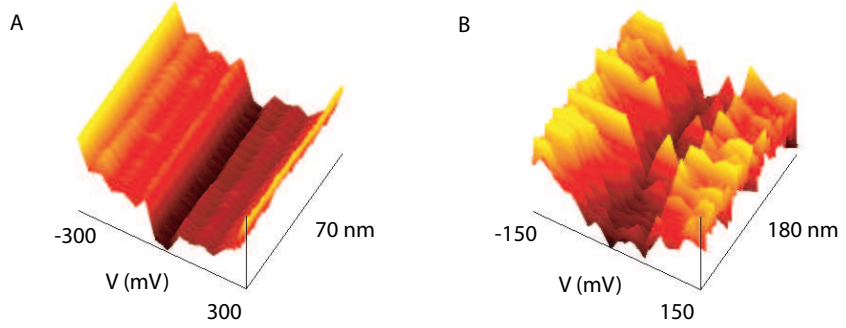


Figure 3.9: A. Three dimensional  $\frac{dI}{dV}$  plots as a function of the bias voltage and the position of the carbon nanotube tip on a  $\text{YBa}_2\text{Ca}_3\text{O}_{6+x}$  surface at 15 K . The conductivity peaks don't change as the tip moves. The superconducting energy gap ( $\Delta_{SC}$ ) can be calculated from the difference between the central blockade region size and the other blockade region sizes. B. Similar plot for Pr-Ir tip- $\text{Bi}_2\text{Sr}_2\text{CaCu}_2\text{O}_{8+x}$  system at 36K without CB behavior.

structure of the sample, we can use the CITS technique. Current imaging tunneling spectroscopy (CITS) is a powerful STM technique which provides not only topographic but also spectroscopic information. CITS was especially successful in the STM studies of high- $T_C$  surfaces [28] [29] [30]. Normally, STM tips are metal tips with simple band structures and we can interpret CITS data as a characteristic of the sample alone. In our CNT tip's case, however, we had to consider single electron tunneling in double-junctioned island system due to the strong tip-dependent I-V. Also special care was needed because CNT tips showed strong asymmetric I-V's, that is, diode-like behavior in some cases which caused large current fluctuations or a tip crash with a specific sign of the bias. Usually, a positive bias worked fine. After some experience with these unusual nanosized tips, it was possible to get atomic resolution simultaneously with the Coulomb blockade I-V curves at each position. From

this map, we can extract new information which cannot be gathered from the CITS with conventional STM tips. In orthodox theory, periodicity of the steps in Coulomb blockade depends on the capacitance  $C_{\Sigma} = C_1 + C_2$ , which in our case, largely depends on the tip-sample capacitance  $C_2$ . Also the CB features are shifted by the charge  $Q_0$  induced in the single electron island [4]. This  $Q_0$  is given by a product of the capacitance and additional voltage. A good example is single electron transistor (SET) where  $Q_0 = C_{gate}V_{gate}$ . Although CNT STM tips do not have a gate lead directly connected to the nanotubes, if fixed charge, therefore potential offset, on the scanning surface varies, we can detect it with a great resolution from the change in local I-V spectra. In other words, by taking CITS data with a double-barrier-CNT STM tip, we can have a two dimensional charge(or potential) distribution and capacitance map as well as topographic information simultaneously. Naturally, we examined this possibility.

In an actual CITS run, an I-V sweep is performed at every pixel in real time as a topographic scan is performed.  $\frac{dI}{dV}$  was calculated from the I-V map thus obtained. In constant height mode, the tip-sample distance can vary due to the slope of the sample, which can greatly affect the capacitance between tip and sample,  $C_2$ . Instead, we chose constant current mode for the topographic scan with a bias voltage far from the blockade region. Fig. 3.10-B shows plot of  $\frac{dI}{dV}$  along one scan line from CITS data from the CNT nanotube tip-HOPG system. The x axis is the spatial distance, y axis is the bias voltage  $V_d$ , and brightness is the conductivity  $\frac{dI(x,V)}{dV}$ . Also, the topographic profile and image

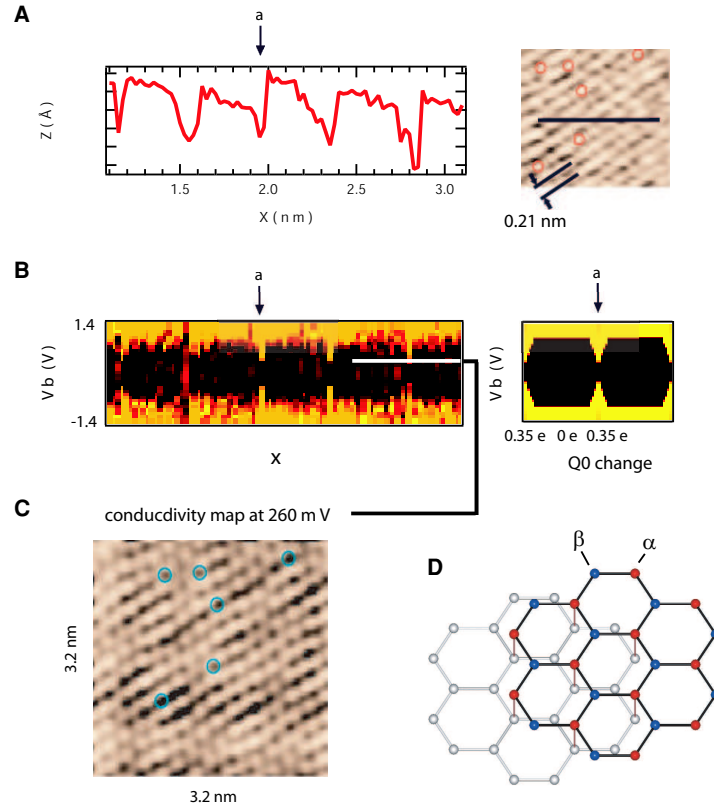


Figure 3.10: **(A)** Topographic profile corresponding to the black line on the image of HOPG on the right. The atomic rows are 2.1 Å apart. Note that red circles in the topographic image are on the hills. Feedback bias voltage was 1.4 V which is far from the central blockade region, and the tunneling current was 70 pA. Temperature was 80 K. **(B)** Two dimensional plot of  $\frac{dI}{dV}$  of CNT nanotube STM tip - HOPG system as a function of position and bias voltage. The I-V curve was taken along the line in A and  $\frac{dI}{dV}$  was calculated from it. At the topographic dip (a), the blockade region gets narrow. On the right, a similar plot of the simulation result is shown. For the simulation parameters,  $C_{\Sigma} = 2.0 \times 10^{-19}$ ,  $R_1 = R_2 = 1.0 \times 10^8$ ,  $T = 80K$  were used.  $Q_0$  is set to oscillate between  $0e$  and  $0.35e$ . **(C)** Conductivity plot as a function of x and y at the bias voltage of 260 mV. This bias is where the discrete conductivity peak can be mapped. Individual filled states can be seen. Note that blue circles are on valleys even though their positions are identical to the red circles in A. **(D)** Crystal structure of graphite surface. Due to the strong site asymmetry, triangular sublattice is visible in STM topography (  $\alpha$  and  $\beta$  sites ).

are shown in fig. 3.10-A where the black bar in the topographic image designates the line along which the  $\frac{dI}{dV}$  data was taken for the plot in B. Only atomic rows were visible in topography due to high voltage and small current. Individual I-V characteristic showed CB behavior: the dark area in the conductivity plot is the blockaded energy region. Comparing these two graphs, we found that the blockade regions get larger at the maxima of the topography, and vice versa. The smaller diagram is the simulation result where the same  $R_1$  and  $R_2$  values were assumed since the  $\frac{dI}{dV}$  plot is symmetric around zero bias, and from the fitting in fig. 3.7-B, it is possible to have such a high resistance in  $R_1$ . The narrowest blockade regions in the simulation correspond to  $Q_0 = +0.35e$  and the broadest to  $Q_0 = 0$ . Since the bias voltage used for the feedback in topography was +1.4V, the maxima of topography mean empty states where the electrons tunnel into those states [43]. These empty states are also known as  $\alpha$  sites [42] and we can selectively image filled( $\beta$ ) or empty( $\alpha$ ) sites by changing polarity of the bias if we use a larger( $\geq 500$  mV) bias. Therefore, at the minima (filled sites),  $Q_0$ (charge induced in the CNT) should be larger than  $Q_0$  at the maxima(empty sites). The sharper the topographic minimum is, the narrower the CB gap is, because at the sharper topographic minimum, electric field felt by CNT tip can be stronger and thus induce more  $|Q_0|$  than other positions. If we rearrange the CITS data, we can get a tunneling conductivity map at each bias voltage. Around  $V_b = 260mV$ (white line in fig. 3.10-B), conductivities at the site of narrow CB regions(e.g., a) are much higher than others. In fig. 3.10-C, the conductivity map at this bias voltage is shown.

From the above argument, higher conductivity peaks in the map C should be located in the dips in the topography which indeed is the case. Each 6 pairs of red and blue circles in topography and conductivity map are at the same positions, but circles in fig. 3.10-C are on the valleys while circles in 3.10-A are on the hills. Individual filled states are also resolved more clearly due to the sharp contrast of conductivity peaks at 260 mV as shown in fig. 3.10-B.

By decreasing the tip-sample distance, we can expect a greater effect of the sample surface on the CNT STM tip. In fig. 3.11-A, the coulomb peak features change as the tip moves along the scan line differently from that in fig. 3.10. The three dimensional topography is also shown in B with the positions of a, b, c. In Fig. 3.11-A, wrinkle-like features, which are the coulomb staircase conductivity peaks, move up and down in parallel fashion, not in a mirror image pattern as in fig. 3.10. This can be understood by a simple simulation as shown in fig. 3.11-C where asymmetric resistance values are used for  $R_1$  and  $R_2$  values. The horizontal axis is the change of  $Q_0$  and the vertical axis is the bias voltage  $V_b$ . In the first simulation,  $Q_0$  fluctuates mildly within  $\pm 0.4e$  range. Note that in fig. 3.10, the CB gap changed symmetrically, not in a parallel way and the change in  $Q_0$  was within only  $\sim 3.5e$ , where feedback bias was 1.4 V and tip-sample distance was much larger than that of fig. 3.11. In the second simulation,  $Q_0$  is set to change rapidly and shows similar features near b in 3.11. At b, the positive slope of the CB peak change along the x axis agrees with the fact that in negative sample bias, a maximum in the topography corresponds to the filled states, which induce positive  $Q_0$



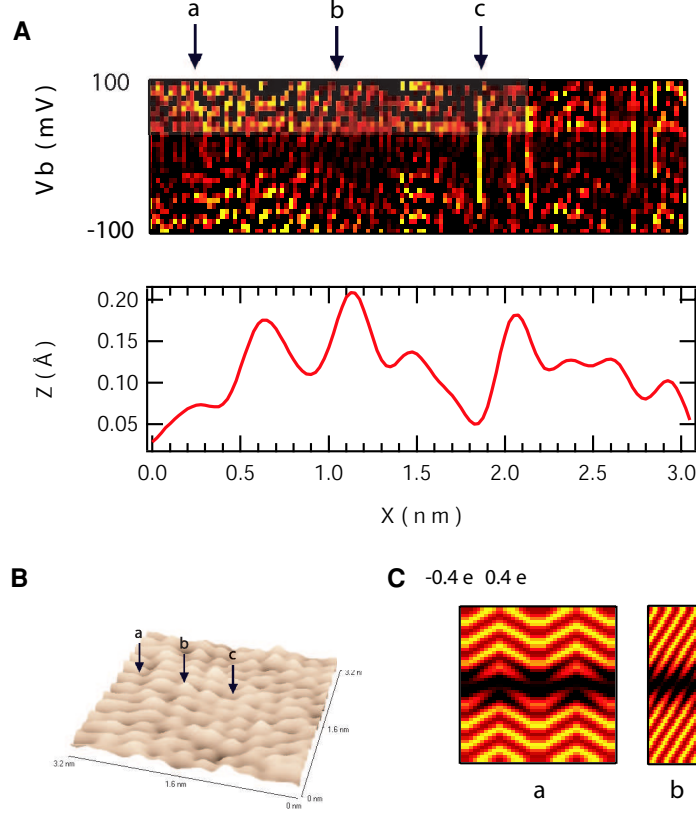


Figure 3.11: **(A)** Two dimensional plot of  $\frac{dI}{dV}$  of CNT nanotube STM tip - HOPG system as a function of position and bias voltage. Also shown is the topographic profile corresponding to the same scan line. **(B)** 3D topographic image where positions a, b, c are indicated. The bias voltage for the feedback in constant current topography was -40 mV and temperature was 83 K. b is at the top of an atom, c is at the dip. **(C)** Simulation result showing  $\frac{dI}{dV}$  vs.  $Q_0$ . At a,  $Q_0$  changes two cycles of  $-0.4e \rightarrow 0.0e \rightarrow 0.4e \rightarrow 0.0e \rightarrow -0.4e$ . At b.,  $Q_0$  is set to rapidly change in one direction. Due to single electron tunneling, whenever  $Q_0$  change exceeds  $0.5e$ , single electron tunneling occurs and  $Q_0$  is set back to  $-0.5e$ . Parameters for the simulations are :  $C_\Sigma = 4.3 \times 10^{-18}$ ,  $R_1 = 5.0 \times 10^6$ ,  $R_2 = 8.5 \times 10^8$ ,  $T = 83K$ . Comparing the simulation results to the experimental results in A, it can be seen that  $Q_0$  change is related to the electronic structure of the HOPG surface.

in the island by the same argument as before, and as the tip approaches a pinnacle,  $Q_0$  changes more than  $1e$ . When  $Q_0 = (n + \frac{1}{2})e$ , the CB staircase shape is reset to that of  $Q_0 = \frac{e}{2}$ . This can be understood in terms of the equilibrium electrostatic energy of the CB circuit diagram in fig. 3.7-D [73]:

$$E_{eq} = \frac{(Q_0 - ne)^2}{2C_\Sigma} + \text{terms independent of } n, \quad (3.1)$$

$$n = \text{integer},$$

where  $n$  is determined by minimizing the energy  $E_{eq}$ . Namely, the charging energy as a function of  $Q_0$  changes with a periodicity of  $1e$ . The small tip-sample tunneling gap distance resulting from the small bias feedback voltage of -40 mV, which can make the CNT tip prone to the sharply localized electric field from the charge dense area ( $\beta$  carbon atoms) and in turn, we observe a large change of  $Q_0$  (according to the simulation,  $\sim 4.0e$ ). The value of  $Q_0$  here cannot be interpreted directly as the same amount of the surface charge but only the amount proportional to it, since the charge in the single electron island can be induced by the electric field from the static charge on the surface as a combination  $Q_0 = V_s C_2$  where  $V_s$  is the potential due to the surface charge. Each simulation fits well the  $\frac{dI}{dV}$  plot near a and b in fig. 3.11-A respectively. The abnormal conductivity peak at the position c, which is the topographic minimum (filled state), may indicate that nanotube tip has interacted more strongly with the sample.

Two dimensional mapping of the CB behavior in this case is not as straightforward as in fig. 3.10 since we need to measure the rate of the change

of  $Q_0$ . However, since the conductivity peak has periodicity related to the  $C_\Sigma$ , we can think of the fourier transform. In fig. 3.12, an topographic STM image(A) and a profile(C) is shown, where the profile is taken along the line  $x_1, x_2$  which passes through all the  $\alpha, \beta$  sites and the center of the honeycomb. The blue dots which designate the peak positions in A can be identified as filled( $\beta$ ) site, since we are using a negative bias voltage of -40mV, at which bias range it is known that the filled sites have larger corrugation than empty states independent of the polarity of the bias [43]. In fig. 3.12-B, squared amplitude of the fast fourier transformed(FFT [74])  $\frac{dI}{dV}$  is shown along the line  $x_1, x_2$ . The horizontal axis is the spatial position and the vertical axis is the frequency  $f_v$ , which has the dimension of the reciprocal of the potential difference,  $f_v = \frac{1}{V}$ . The center of the vertical axis corresponds to zero frequency and the amplitude is even since the original conductivity is a real function. Since the capacitance of the single electron island is given by  $C_\Sigma = \frac{e}{\Delta V_{CB}}$  where  $\Delta V_{CB}$  is the CB staircase step size in V, we can directly find  $C_\Sigma$  from the peak positions in fig. 3.12-B. Along the white line at  $f_{vCB}$ , peak positions correspond to the empty( $\alpha$ ) sites which can be seen more easily by the 2D plot of the squared fourier amplitude at this frequency in fig. 3.12-D. Red dots are found to be the empty site by overlapping them with blue dots (E) and comparing to the topographic profiles. This frequency  $f_{vCB}$  designates the dominant CB oscillation frequency in  $\frac{dI}{dV}$  curves, and 2D map in D means CB behavior is strong at the empty( $\alpha$ ) sites than other sites. This can be understood by noting, that at the  $\alpha$  sites, conductivity is not as strong as at the  $\beta$

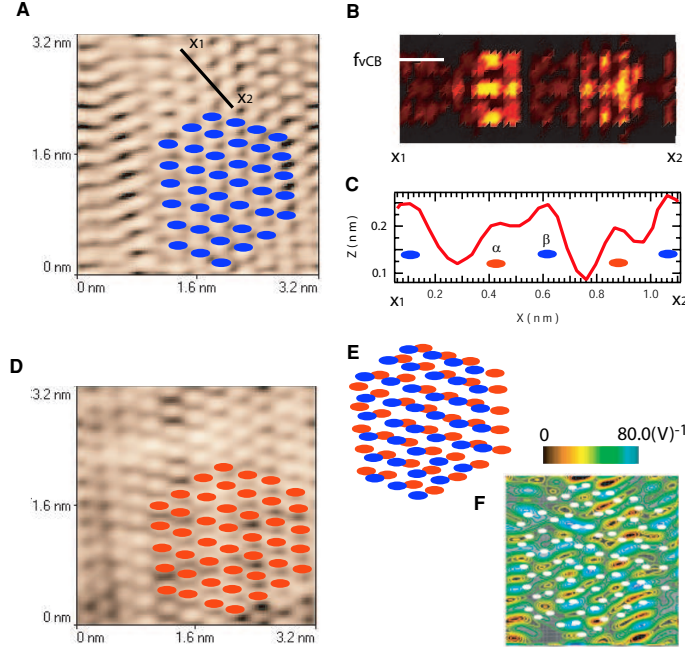


Figure 3.12: Fourier analysis of the CITS data. **(A)** Topographic image during a CITS scan using a carbon nanotube STM tip. Each atom appears to be an ellipse due to the drift of the tip while performing CITS. Blue dots represent peak positions. The bias voltage is -40 mV and  $T = 83\text{K}$ . **(B)** The squared amplitude of the fourier-transformed differential conductance,  $\frac{dI}{dV}(f_v)$  along the black line  $x_1, x_2$  is plotted as a function of the  $f_v \propto \frac{1}{V}$  and the position. **(C)** The topographic profile along the line is also shown, and the color dots designate the asymmetric graphite atoms known as  $\alpha$  site atoms (red), and  $\beta$  site atoms (blue). **(D)** two dimensional plot of amplitude of each Fourier Transformed  $\frac{dI}{dV}$  curve of CITS as a function of  $x, y$  position at the specific frequency designated in B by white line at  $f_v = f_{vCB}$ . Red dots are the peak positions and can be identified as the  $\alpha$  atoms. Refer to the profile in C. **(E)** Aligned together, red dots and blue dots from A and D form the honeycomb lattice which is the actual order of the HOPG bulk. **(F)** The contour plot of the frequency  $f_v m(V^{-1})$  which gives the peak squared fourier amplitude  $|\frac{dI}{dV}(f_v)|^2$  the maximum value, as a function of  $x$  and  $y$ . This map represents the change of the capacitance  $C_2$  between the CNT tip and HOPG surface during scan. The dark areas surrounded by yellow contour lines are the minima which is located inside the honeycomb lattice designated by the white dots. Also notice that most of the maxima (brighter sites surrounded by green lines) corresponds to the  $\alpha$  atom sites.

sites, which makes the resistivity  $R_2$  higher and the ratio  $\frac{R_1}{R_2}$  smaller. From fig. 3.7, we already showed smaller  $\frac{R_1}{R_2}$  results in a sharper CB characteristic. This argument is also consistent with the observation that from the fig. 3.12-B, corresponding peaks exist but are weaker at the filled( $\beta$ ) sites. On the other hand, peak positions are closer to the zero frequency near the sites without atoms(the center of the honeycomb). This variation of the peak position can be interpreted as the change of the capacitance  $C_2$  between the sample and the CNT tip, or in some cases, disappearance of the CB characteristics due to this change. Further, we can use the information of positions of the peaks in the fourier transformed  $|\frac{dI}{dV}(f_v)|^2$  at each pixel to calculate the dominant step size  $V_{CB}$  and in turn, dominant capacitance  $C_\Sigma = \frac{e}{\Delta V_{CB}} = ef_{vmax}$  where  $|\frac{dI}{dV}(f_{vmax})|^2$  has the maximum value. From this argument, it is straightforward that by mapping  $f_{vmax}(x, y)$ , we can map the change of the capacitance between the sample surface and the CNT STM tip as shown in fig. 3.12-F. Indeed, capacitance  $C_2$  values are smaller inside of the honeycomb lattice(white dots) when the map is overlapped with the  $\alpha$ ,  $\beta$  atomic sites in E. This can be attributed to the fact that the DOS is larger around the atomic sites, and therefore,  $C_2$  gets larger whenever the CNT tip is tunneling near high DOS sites.

In conclusion, we observed unusually sharp coulomb staircases using carbon nanotube STM tips, due to the strong asymmetry of the nature of the two junctions on the CNT, and many different I-V curves can be explained in terms of the CB phenomena. Judging from the step size( $E_c$  as large as 145

meV) and the orthodox theory's condition for the CB ( $E_c \gg k_B T$  [4]), it's possible to observe CB in our CNT STM tips even at room temperature ( $k_B T_{RT} \simeq 25 meV$ ). We also used the CITS technique and the two different cases of the charge-sensitive oscillatory  $\frac{dI}{dV}$  curves of the CNT tips and the CITS technique to demonstrate the mapping of the charge distribution and the capacitive variation on the HOPG surface, which we believe opens a new possibility of the microscopy using the CNT nanotube tips without the complicated fabrication processes required in other SETSE probes. Still our CNT STM tip's charge sensitivity needs to be calibrated to give the direct interpretation in terms of the surface charge. We are working on the optimization of the conditions for the carbon nanotube tip growth, and trying to find its relation to the I-V characteristics. Maybe in the future, we can find the conditions for the synthesis of the CNT STM tips with various I-V characteristics which is applicable directly to the CNT device processes.

We can anticipate more possibilities of these CNT STM tips and the technique demonstrated in this report. Considering most of the catalyst for the CNT growth are ferromagnetic, tips for the spin-polarized scanning tunneling microscopy (SP-STM) [75] can be obtained by growing CNT under the magnetic precursor. An ultra sharp CNT SETSE probe can be realized by connecting an additional lead to the CNT tip. The technique to make contact to the CNT can be found in some reports [76]. Recently, spin-resolved STM (SR-STM) using CNT with two ferromagnetic electrodes was suggested [77]. In this context, one can use ferromagnetic metal tip (e.g. Ni) instead of W tip for the

CNT growth and add one additional ferromagnetic electrode to fabricate SR-STM tip. For another possibility, if the single wall carbon nanotube(SWNT) STM tip is available, and temperature is lowered to the 100 mK regime, a lower energy scale due to the spin effect [78] [79] can be utilized to conduct the spin resolved CITS operation. Also if the temperature is lowered below the superconducting  $T_c$ ( $\sim 0.55$  K [80]) of the carbon nanotubes, it would be possible to conduct SIS tunneling experiment and study of the mesoscopic superconductivity.

This work is supported by NSF-DMR 0072834.

## Bibliography

- [1] G. Binnig, H. Rohrer, Ch. Gerber, and E. Weibel. *Appl. Phys. Lett.*, 40:178, 1982.
- [2] G. Binnig, H. Rohrer, Ch. Gerber, and E. Weibel. *Phys. Rev. Lett.*, 49:57, 1982.
- [3] D. J. Thouless. *Phys. Rev. Lett.*, 39:1167, 1977.
- [4] M. H. Devoret and H. Grabert. *Single Charge Tunneling-Coulomb blockade phenomena in nanostructures*. Plenum Press, New York, 1992.
- [5] D. V. Averin and K. K. Likharev. *Mesoscopic Phenomena in Solids-Modern problems in condensed matter sciences*, volume 30. North-Holland, Amsterdam, 1991.
- [6] S. Iijima and T. Ichihashi. *Nature*, 363:603, 1993.
- [7] H. W. Kroto, J. R. Heath, S. C. O'Brien, R. F. Culr, and R. E. Smalley. *Nature*, 318:162, 1985.
- [8] M. Di Ventra and S. T. Pantelides. *Phys. Rev. B*, 59:5320, 1999.
- [9] G. Doyen, D. Drakova, and M. Scheffler. *Phys. Rev. B*, 47:9778, 1993.
- [10] J. Cerdá and M. A. Van Hove. *Phys. Rev. B*, 56:15885, 1997.



- [11] R. Wiesendanger and H. J. Güntherodt, editors. *Scanning Tunneling Microscopy III - Theory of STM and related scanning probe methods*. Springer-Verlag, Berlin, 1993.
- [12] J. Tersoff and D. R. Hamann. *Phys. Rev. Lett.*, 50:1998, 1983.
- [13] J. Tersoff and D. R. Hamann. *Phys. Rev. B*, 31:805, 1985.
- [14] J. Bardeen. *Phys. Rev. Lett.*, 6:57, 1961.
- [15] C. J. Chen. *Introduction to scanning tunneling microscopy*. Oxford University Press, New York, Oxford, 1993.
- [16] M. P. Marder. *Condensed Matter Physics, corrected printing*. John Wiley & Sons, Inc., New York, N. Y., 2000.
- [17] R. Landauer. *IBM J. Res. Dev.*, 1:223, 1957.
- [18] R. Landauer. *IBM J. Res. Dev.*, 32:306, 1988.
- [19] C. W. J. Beenakker and H. van Houten. *Solid State Physics-Advances in Research and Applications*, volume 44. Academic Press, INC, Boston, 1991.
- [20] S. Datta. *Electronic transport in mesoscopic systems*. Cambridge University Press, Cambridge, U.K., 1995.
- [21] Y. Imry. *Directions in condensed matter physics*, volume 1. World Scientific, Singapore, 1986.

- [22] C. W. J. Beenakker. *Rev. Mod. Phys.*, 69:731, 1997.
- [23] D. Ferry and S. M. Goodnick. *Transport in Nanostructures*. Cambridge University Press, Cambridge, U.K., 1997.
- [24] K. K. Likharev. *Proc. IEEE*, 87:606, 1999.
- [25] K. K. Likharev. *IBM J. Res. Dev.*, 32:144, 1988.
- [26] A. L. de Lozanne, S. A. Elrod, and C. F. Quate. *Phys. Rev. Lett.*, 54:2433, 1985.
- [27] D. P. E. Smith and G. Binnig. *Rev. Sci. Instrum.*, 88:2630, 1986.
- [28] H. L. Edwards, D. J. Derro, A. L. Barr, J. T. Markert, and A. L. de Lozanne. *Phys. Rev. Lett.*, 75:1387, 1995.
- [29] S. H. Pan, J. P. O’Neal, R. L. Badzey, C. Chamon, H. Ding, J. R. Engelbrecht, Z. Wang, H. Eisaki, S. Uchida, A. K. Gupta, K.-W. Ng, E. W. Hudson, K. M. Lang, and J. C. Davis. *Nature*, 413:282, 2001.
- [30] D. J. Derro, E. W. Hudson, K. M. Lang, S. H. Pan, J. C. Davis, J. T. Markert, and A. L. de Lozanne. *Phys. Rev. Lett.*, 88:097002, 2002.
- [31] H. F. Hess, R. B. Robinson, and J. V. Waszczak. *Phys. Rev. Lett.*, 64:2711, 1990.
- [32] D. M. Eigler and E. K. Schwiezer. *Nature*, 344:524, 1990.

- [33] C. Joachim, J. K. Gimzewski, R. R. Schlittler, and C. Chavy. *Phys. Rev. Lett.*, 74:2102, 1995.
- [34] J. W. G. Wildöer, L. C. Venema, A. G. Rinzier, R. E. Smalley, and C. Dekker. *Nature*, 391:59, 1998.
- [35] T. W. Odom, J. Huang, P. Kim, and C. M. Lieber. *Nature*, 391:62, 1998.
- [36] C. Wittneven, R. Dombrowski, S. H. Pan, , and R. Wiesendanger. *Rev. Sci. Instrum.*, 68:3806, 1997.
- [37] B. C. Stipe, M. A. Rezaei, and W. Ho. *Rev. Sci. Instrum.*, 70:137, 1999.
- [38] S. H. Pan, E. W. Hudson, and J. C. Davis. *Rev. Sci. Instrum.*, 70:1459, 1999.
- [39] Shuheng Pan. *An Ultra High Vacuum Low Temperature Scanning Tunneling Microscope and It's Applications to High- $T_C$  Superconductors and Quasi One-Dimensional Organic Conductors*. PhD thesis.
- [40] Henry L. Edwards. *Scanning-Tunneling Microscopy and Spectroscopy of  $\text{YBa}_2\text{Ca}_3\text{O}_{6+x}$  and the Quantum-Dot Thermoelectric Refrigerator*. PhD thesis.
- [41] Frank Pobell. *Matter and Methods at Low Temperatures*. Springer-Verlag, Berlin-Heidelberg, 1992.
- [42] D. Tománek and S. G. Louie. *Phys. Rev. B*, 37:8327, 1988.

- [43] S. Gwo and C. K. Shih. *Phys. Rev. B*, 47:13059, 1993.
- [44] J. E. Hoffman, K. McElroy, D. H. Lee, K. M. Lang, H. Eisaki, S. Uchida, and J. C. Davis. *Science*, 297:1148, 2002.
- [45] S. Sugita, T. Watanabe, and A. Matsuda. *Phys. Rev. B*, 62:8715, 2000.
- [46] C. K. Shih, R. M. Feenstra, J. R. Kirtley, and G. V. Chandrashekhar. *Phys. Rev. B*, 40:2682, 1989.
- [47] C. K. Shih, R. M. Feenstra, and G. V. Chandrashekhar. *Phys. Rev. B*, 43:7913, 1991.
- [48] S. Misra, S. Oh, D. J. Hornbaker, T. DiLuccio, J. N. Eckstein, and A. Yazdani. *Phys. Rev. Lett.*, 89:087002, 2002.
- [49] J. E. Hoffman, E. W. Hudson, K. M. Lang, V. Madhavan, H. Eisaki, S. Uchida, and J. C. Davis. *Science*, 295:466, 2002.
- [50] P. G. Collins, A. Zettl, H. Bando, A. Thess, and R. E. Smalley. *Science*, 278:100, 1997.
- [51] H. Dai, J. H. Hafner, A. G. Rinzler, D. T. Colbert, and R. E. Smalley. *Nature*, 384:147, 1996.
- [52] H. Nishijima, S. Kamo, S. Akita, and Y. Nakayama. *Appl. Phys. Lett.*, 74:4061, 1999.
- [53] I. H. Musselman and P. E. Russell. *J. Vac. Sci. Technol. A*, 8:3558, 1990.

- [54] M. M. J. Treacy, T. W. Ebbesen, and J. M. Gibson. *Nature*, 381:678, 1996.
- [55] M. Dresselhaus, G. Dresselhaus, and P. C. Eklund. *Science of Fullerenes and Carbon Nanotubes*. Academic Press, San Diego, 1996.
- [56] P. M. Ajayan. *Chem. Rev.*, 99:1787, 1999.
- [57] J. H. Hafner, M. J. Bronikowski, B. R. Azamian, P. Nikolaev, A. G. Rinzler, D. T. Colbert, K. Smith, and R. E. Smalley. *Chem. Phys. Lett.*, 296:195, 1998.
- [58] T. Yamada. *Appl. Phys. Lett.*, 78:1739, 2001.
- [59] C. Tiusan, M. Chshiev, A. Iovan, V. d. Costa, D. Stoeffler, T. Dimopoulos, and K. Ounadjela. *Appl. Phys. Lett.*, 79:4231, 2001.
- [60] M. Chshiev, D. Stoeffler, A. Vedyayev, and K. Ounadjela. *Europhys. Lett.*, 58:257, 2002.
- [61] T. W. Odom et al. *J. Phys. Chem. B*, 104:2794, 2000.
- [62] P. Delsing, K. K. Likharev, L. S. Kuzmin, and T. Claeson. *Phys. Rev. Lett.*, 63:1861, 1989.
- [63] P. L. McEuen, E. B. Foxman, U. Meirav, M. A. Kastner, Y. Meir, and N. S. Wingreen. *Phys. Rev. Lett.*, 66:1926, 1991.
- [64] P. J. M. van Bentu, R. T. M. Smokers, and H. van Kempen. *Phys. Rev. Lett.*, 60:2543, 1988.

- [65] A. E. Hanna and M. Tinkham. *Phys. Rev. B*, 44:5919, 1991.
- [66] M. J. Yoo, T. A. Fulton, H. F. Hess, R. L. Willett, L. N. Dunkleberger, R. J. Chichester, L. N. Pfeiffer, and K. W. West. *Science*, 276:579, 1997.
- [67] N. B. Zhitenev, T. A. Fulton, A. Yacoby, H. F. Hess, L. N. Pfeiffer, and K. W. West. *Nature*, 404:473, 2000.
- [68] M. Bockrath, D. H. Cobden, P. L. McEuen, N. G. Chopra, A. Zettle, A. Thess, and R. E. Smalley. *Science*, 275:1922, 1997.
- [69] M. T. Woodside and P. L. McEuen. *Science*, 296:1098, 2002.
- [70] S. J. Tans, M. H. Devoret, H. Dai, A. Thess, R. E. Smalley, L. J. Geerligs, and C. Dekker. *Nature*, 386:474, 1997.
- [71] Z. Yao, H. W. C. Postma, L. Balents, and C. Dekker. *Nature*, 402:273, 1999.
- [72] H. L. Edwards, J. T. Markert, and A. L. de Lozanne. *Phys. Rev. Lett.*, 69:2967, 1992.
- [73] M. A. Kastner. *Rev. Mod. Phys.*, 64:849, 1991.
- [74] W. H. Press, S. A. Teukolsky, W. T. Vetterling, and B. P. Flannery. *Numerical Recipes in C, 2nd Ed.* Cambridge University Press, Cambridge, U.K., 1992.
- [75] O. Pietzsch, A. Kubetzka, M. Bode, and R. Wiesendanger. *Science*, 292:2053, 2001.

- [76] P. Kim and C. M. Lieber. *Science*, 286:2148, 1999.
- [77] D. Orgassa, G. J. Mankey, and H. Fujiwara. *Nanotechnology*, 12:281, 2001.
- [78] D.H. Cobden, M. Bockrath, and P. L. McEuen. *Phys. Rev. Lett.*, 81:681, 1998.
- [79] C. Kane. *Phys. Rev. Lett.*, 79:5086, 1997.
- [80] M. Kociak, A. Y. Kasumov, S. Gueron, B. Reulet, I. I. Khodos, Y. B. Gorbatov, V. T. Volkov, L. Vaccarini, and H. Bouchiat. *Phys. Rev. Lett.*, 86:2416, 2001.
- [81] H. F. Hess, R. B. Robinson, R. C. Dynes, Jr. J. M. Valles, and J. V. Waszczak. *Phys. Rev. Lett.*, 62:214, 1989.
- [82] N. Nishiguchi. *Phys. Rev. B*, 65:035403, 2001.
- [83] H. W. C. Postma, T. Teepen, Z. Yao, M. Grifoni, and C. Dekker. *Science*, 293:76, 2001.
- [84] J. Haruyama, I Takesue, and T Hasegawa. *Appl. Phys. Lett.*, 81:3031, 2002.
- [85] S. Iijima. *Nature*, 354:56, 1991.
- [86] A. Garg, J. Han, and S. B. Sinnott. *Phys. Rev. Lett.*, 81:2260, 1998.

# Vita

Jinho Lee was born in Seoul, Korea on December 19, 1969, the son of Sang-Moo Lee and Seonja Kim. He received the Bachelor of Science degree in Physics from Seoul National University, Seoul, Korea and continued his study in the same university as a graduate student. He worked on design and construction of DC multi-target magnetic sputtering system, and also synthesis and transport measurement of high- $T_C$  multi-layer thin films and Josephson junctions made of the films. He earned a Master of Science degree in 1992 with a thesis, *Fabrication and Physical Properties of  $YBa_2Ca_3O_{6+x}$  /  $PrBa_2Ca_3O_{6+x}$  /  $YBa_2Ca_3O_{6+x}$  SNS Multi-layer Josephson Junctions*. After one and a half years of military service in Korean Army, he came to the United States to enter the graduate school of the University of Texas at Austin in the Fall of 1995. He was elected to the academic honor societies of Phi Kappa Phi and Sigma Xi in 1996 and 1997 respectively, and sponsored by Korean Bureau of Education Scholarship program from 1995 to 1998.

Permanent address: 1650 w. 6th st. APT K  
Austin, Texas 78703

This dissertation was typeset with  $\text{\LaTeX}^\dagger$  by the author.

---

<sup>†</sup> $\text{\LaTeX}$  is a document preparation system developed by Leslie Lamport as a special version of Donald Knuth's  $\text{\TeX}$  Program.